Quantum wavepacket *ab initio* molecular dynamics: Generalizations using an extended Lagrangian treatment of diabatic states coupled through multireference electronic structure

Xiaohu Li and Srinivasan S. Iyengar[a)]
Department of Chemistry and Department of Physics, Indiana University, 800 E. Kirkwood Ave, Bloomington, Indiana 47405, USA

We present a generalization to our previously developed quantum wavepacket *ab initio* molecular dynamics (QWAIMD) method by using multiple diabatic electronic reduced single particle density matrices, propagated within an extended Lagrangian paradigm. The Slater determinantal wavefunctions associated with the density matrices utilized may be orthogonal or nonorthogonal with respect to each other. This generalization directly results from an analysis of the variance in electronic structure with quantum nuclear degrees of freedom. The diabatic electronic states are treated here as classical parametric variables and propagated simultaneously along with the quantum wavepacket and classical nuclei. Each electronic density matrix is constrained to be N-representable. Consequently two sets of new methods are derived: extended Lagrangian-QWAIMD (xLag-QWAIMD) and diabatic extended Lagrangian-QWAIMD (DxLag-QWAIMD). In both cases, the instantaneous potential energy surface for the quantum nuclear degrees of freedom is constructed from the diabatic states using an on-the-fly nonorthogonal multireference formalism. By introducing generalized grid-based electronic basis functions, we eliminate the basis set dependence on the quantum nucleus. Subsequent reuse of the two-electron integrals during the on-the-fly potential energy surface computation stage yields a substantial reduction in computational costs. Specifically, both xLag-QWAIMD and DxLag-QWAIMD turn out to be about two orders of magnitude faster than our previously developed time-dependent deterministic sampling implementation of QWAIMD. Energy conservation properties, accuracy of the associated potential surfaces, and vibrational properties are analyzed for a family of hydrogen bonded systems. © *2010 American Institute of Physics*. [doi:10.1063/1.3504167]

I. INTRODUCTION

In a series of recent publications,[1–9] we have introduced a methodology that accurately computes quantum dynamical effects in a subsystem while simultaneously treating the motion of the surrounding atoms and changes in electronic structure. The approach is quantum-classical[10–17] and involves the synergy between a time-dependent quantum wavepacket description and *ab initio* molecular dynamics. As a result, the approach is called quantum wavepacket *ab initio* molecular dynamics (QWAIMD). Since the quantum dynamics is performed on Cartesian grids, the predominant bottleneck is the computation of the grid-based, time-dependent electronic structure potential and gradients generated by the motion of the classical nuclei. This limitation is partially surmounted through the introduction of a time-dependent deterministic sampling (TDDS) technique,[3,4] which when combined with numerical methods such as an efficient wavelet compression[4,18–23] scheme and low-pass filtered Lagrange interpolation,[4,24–26] provides computational gains of many orders of magnitude. QM/MM generalizations to QWAIMD have also been completed.[5] We have utilized QWAIMD to compute vibrational properties of hydrogen bonded clusters inclusive of quantum nuclear effects[4] and have also adopted the method to study hydrogen tunneling in enzyme active sites.[6,7] The quantum dynamics scheme in QWAIMD has also been used to develop a technique known as multistage *ab initio* wavepacket dynamics (MSAIWD) to treat the electronic dynamics and structure of open, nonequilibrium systems.[8] The approach is being generalized to treat extended systems[27] for condensed phase simulations; a biased QWAIMD formalism to sample rare events is also currently being developed.[28]

Significant challenges remain and a few of these are as follows: At present it is only possible to study QWAIMD using moderately accurate electronic structure methods, such as hybrid density functional theory. More accurate, post-Hartree–Fock calculations conducted on-the-fly with QWAIMD are currently prohibitive. Due to the expense involved in on-the-fly dynamics, currently it is only possible to treat one quantum nuclear particle that is coupled to a set of classical particles, and generalizations to multiple quantum dynamical particles are in progress. Dynamics of the order of several picoseconds is possible but longer time-scale dynamics is expensive. This publication takes an important step in the direction of (a) performing QWAIMD simulations with efficient on-the-fly post-Hartree–Fock calculations and (b)

a)Electronic mail: iyengar@indiana.edu.

further reducing the computational cost involved in QWAIMD calculations to facilitate longer time-scale dynamics.

This paper is organized as follows: In Sec. III, we analyze the computational expense involved in QWAIMD using a principal component analysis of the variance in electronic structure on the quantum nuclear grid. This analysis leads us to a technique that helps reduce the number of on-the-fly calculations, beyond what is already possible with time-dependent deterministic sampling. Consequently, in Sec. IV, an extended Lagrangian generalization to QWAIMD is provided which allows multiple single particle electronic density matrices to be simultaneously propagated with quantum/classical dynamics of nuclei. The resultant potential energy surface is computed using a nonorthogonal (configuration interaction) CI-type method[29–36] as discussed in Sec. IV A. When the individual single particle electronic density matrices are interpreted as diabatic states, the density matrices remain independent of the quantum nuclear degrees of freedom. This in turn allows the reuse of two-electron integral terms across all quantum nuclear grid points while computing the potential surface and produces large computational savings as discussed in Sec. IV B, with little loss in accuracy as shown in the numerical benchmarks, Sec. V. Conclusions are given in Sec. VI. For completeness, QWAIMD is briefly reviewed in Sec. II, with further details in the references provided above. Before we proceed we note that four different acronyms are used in this publication. We define these here and also in the sections of first appearance. The methods extended Lagrangian-QWAIMD (xLag-QWAIMD) and diabatic extended Lagrangian-QWAIMD (DxLag-QWAIMD) are introduced in Sec. IV and refer to the generalization of QWAIMD using the extended Lagrangian formalism. The terms "full-QWBOMD" and "TDDS-QWBOMD" are utilized to differentiate from the above and refer to the previously described implementation of QWAIMD[1–5] that does not utilize an extended Lagrangian formalism.

II. MAIN FEATURES OF QWAIMD AND ASSOCIATED LIMITATIONS

For completeness, we state a few key features of QWAIMD. Further details can be found in Refs. [1–5]. In QWAIMD, starting from the time-dependent Schrödinger equation, a system is partitioned into three sections based on complexity. Subsystem A comprises particles, such as protons, that display critical quantum dynamical effects. Subsystems B and C comprise the surrounding nuclei and electrons that dynamically influence subsystem A. While particles in subsystem A are studied using time-dependent Schrödinger equation, subsystems B and C are treated simultaneously using *ab initio* molecular dynamics.

The quantum dynamical propagation is performed by using Trotter factorization[37,38] where the free-propagator is approximated using the distributed approximating functional (DAF),[1,2,39–41]

$$\langle R_{QM}|\exp\left\{-\frac{\imath K \Delta t_{QM}}{\hbar}\right\}|R'_{QM}\rangle_{DAF}$$
$$= \frac{1}{\sigma(0)}\exp\left\{-\frac{(R_{QM}-R'_{QM})^2}{2\sigma(\Delta t_{QM})^2}\right\}$$
$$\times \sum_{n=0}^{M_{DAF}/2}\left(\frac{\sigma(0)}{\sigma(\Delta t_{QM})}\right)^{2n+1}$$
$$\times\left(\frac{-1}{4}\right)^n\frac{1}{n!}(2\pi)^{-1/2}H_{2n}\left(\frac{R_{QM}-R'_{QM}}{\sqrt{2}\sigma(\Delta t_{QM})}\right). \quad (1)$$

Here $\{\sigma(\Delta t_{QM})\}^2 = \sigma(0)^2 + \imath\Delta t_{QM}\hbar/M_{QM}$, $\{H_{2n}(x)\}$ are even order Hermite polynomials (note that the arguments for the Hermite polynomials and the Gaussian function, $(R_{QM} - R'_{QM}/\sqrt{2}\sigma(\Delta t_{QM}))$, are complex in general), R_{QM} represents the quantum mechanical degrees of freedom, and the parameters M_{DAF} and σ are chosen as in previous studies[1,40] for a best compromise between accuracy and efficiency. Specifically, in all calculations performed here $M_{DAF}=60$ (that is all even Hermite polynomials up to order 60 are used) and $\sigma/\Delta=2.5742$, where Δ is the grid spacing. Multidimensional forms of the above propagator are obtained through direct product.

The evolution of the classical nuclei involves the wavepacket averaged Hellmann–Feynman forces obtained from electronic structure calculations carried out on the discrete wavepacket grid. To minimize the number of electronic structure calculations carried out on the grid, while directing their placement for maximum effect, in Refs. [3] and [4], we introduced the adaptive, TDDS function

$$\omega_{TDDS}(R_{QM}) \propto \frac{[\tilde{\rho} + 1/I_\chi] \times [\tilde{V}' + 1/I_{V'}]}{\tilde{V} + 1/I_V}, \quad (2)$$

which is proportional to the wavepacket density, $\tilde{\rho}$, the potential gradients, $\tilde{V}'$, and inversely proportional to the grid potential, $\tilde{V}$. As shown in Ref. [3], the choice of parameters, $I_\chi=1$, $I_{V'}=3$, and $I_V=1$, retains significant distribution in both the classically allowed (minimum energy regions) and classically forbidden (classical turning point) regions of the potential and leads to a large reduction in computational cost, with little perceivable loss in accuracy. The rationale behind the choice of these parameters can be qualitatively noted from the following arguments with details in Ref. [3]. The functions $\tilde{\rho}$, $\tilde{V}'$, and $\tilde{V}$ are shifted and normalized[3] and hence, (a) minimum energy regions of the potential surface are characterized by low potential energy, low gradient and relatively high wavepacket distribution, while (b) quantum tunneling (or classical turning point) regions of the potential are approximately characterized by moderately large values of the potential, high gradients, and smaller wavepacket values. When one enforces the condition that the TDDS function must be approximately equal in these two situations for minimal bias between the classically allowed and classically forbidden regions, it is found that $I_\chi=1$, $I_{V'}=3$, and $I_V=1$ provides the lowest order solution satisfying these considerations.[3] (Higher order solutions further increase the sampling in the classically forbidden regions.) In addition to

these formal considerations, the parameters have been numerically tested in Ref. 3 for a set of 70 analytical and numerical potentials and the results are found to be consistent with the above physical arguments. The TDDS function is evaluated at every instant in time to determine the grid points where the potential and gradients will be evaluated for the next time-step. Details on the TDDS algorithm as well as its connections to Bohmian mechanics and the WKB approximation are discussed in Refs. 3 and 4. This technique allows large scale reductions in computation time (by several orders of magnitude), with little perceivable loss in accuracy.

In Ref. 4, the above formalism has been benchmarked for accuracy in computing vibrational properties in hydrogen bonded clusters. Specifically, the ClHCl⁻ system was treated since it provides significant challenges for accurate modeling of electron-nuclear coupling.[4,42–44] In Ref. 4 the TDDS implementation of QWAIMD was found to accurately reproduce the experimental spectrum at limited computational cost. The analysis of trajectories is facilitated through the introduction of a novel velocity-flux correlation function.[4] In addition, as noted in the introductory section, QWAIMD has been adopted to study hydrogen tunneling in enzyme active sites[6,7] and QM/MM generalizations to the TDDS implementation of QWAIMD have also been completed.[5] In Ref. 45, the quantum dynamics tools from QWAIMD were used to compute the qualitative accuracy involved in classical *ab initio* molecular dynamics calculations of vibrational spectra in hydrogen bonded systems.

In Ref. 46, we have introduced further modifications to the TDDS function, using the concept for Shannon's information entropy.[47,48] The associated TDDS functions are also utilized here for (a) placement of grid-based electronic structure basis functions, as discussed in Sec. IV C, and (b) identification of initial conditions for diabatic states as discussed in Sec. IV B 1.

III. THE PRINCIPAL ELECTRONIC STRUCTURE COMPONENTS ON THE QUANTUM NUCLEAR GRID

The electronic structure has explicit dependence on the position of the quantum nuclear grid points, since at each grid point, we obtain the electronic structure using converged wavefunctions. Such electron-nuclear correlation is critical for accurate description of the vibrational properties including quantum nuclear effects.[4,42] However, the extent of such correlation is system dependent and the idea behind TDDS has been to extrapolate the time-dependence of such a correlation utilizing parameters available during dynamics as highlighted above. In this section, we further explore the electron-nuclear coupling through examination of *the principal components of the electronic structure* on the quantum grid. This analysis leads to an alternate approach to further "compress" the electron-nuclear coupling information as discussed in subsequent sections of this paper.

Our goal is to first investigate the "self-similarity" of electronic structure on the quantum grid points. To probe the similarity between different electronic density matrices, we first define a self-similarity metric, or distance measure, between the density matrices,
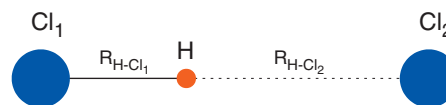

FIG. 1. The parameters R_{H-Cl_1} and R_{H-Cl_2} are defined here and used in Figs. 2–4.

$$\mathbf{S}_{ij} = \frac{1}{N}\mathbf{Tr}[\mathbf{P_i P_j}], \tag{3}$$

where $\mathbf{P_i}$ is the density matrix on grid point i and N is the total number of electrons. When orthonormal density matrices are used, the diagonal elements of this matrix have the property that $\mathbf{S_{ii}} = (1/N)\mathbf{Tr}[(\mathbf{P_i})^2] = 1$, where we have used the idempotency[49] of density matrix. For this case, the off-diagonal elements are bounded as

$$\mathbf{S_{ij}} = \frac{1}{N}\mathbf{Tr}[\mathbf{P_i P_j}] = \frac{1}{N}\sum_{l=1}^{N}\left\{\sum_{k=1}^{N}|\langle\chi_l^j|\chi_k^i\rangle|^2\right\} \le 1, \tag{4}$$

because the quantity $\{\Sigma_{k=1}^{N}|\langle\chi_l^j|\chi_k^i\rangle|^2\}$ is bounded by the length of the vector $|\chi_l^j\rangle$ and is hence less than or equal to 1. An expression similar to Eq. (3) has been employed as a constraint in Ref. 50 to bias the SCF procedure toward nonstandard electronic structure wavefunctions.

Next, the principal components of the electronic structure on the nuclear grid are obtained through singular value decomposition (SVD)[26,51] of the distance measure in Eq. (3) as

$$\mathbf{U^T S V} = \Sigma, \tag{5}$$

where $\mathbf{U}$ and $\mathbf{V^T}$ are orthogonal matrices and Σ is a diagonal singular value matrix. The matrices $\mathbf{U}$ and $\mathbf{V^T}$, in general, form a biorthogonal basis but since $\mathbf{S}$ is a symmetric square matrix, $\mathbf{V} = \mathbf{U}$. The columns of the matrix $\mathbf{V}$ provide a rotation $\{\mathbf{P_i}\} \rightarrow \{\bar{\mathbf{P}}_\mathbf{i}\}$. The number of nonzero singular values, i.e., the dimension of Σ, determines the number of distinct $\bar{\mathbf{P}}_\mathbf{i}$ matrices and hence determines the number of principal components of electronic structure on the quantum nuclear grid.

To showcase the principal components of electronic structure on the quantum grid, we choose our example to be ClHCl⁻, on account of the known challenges this system presents to accurately model electron-nuclear coupling.[4,42–44] The shared proton was chosen to be the quantized particle with the chlorine atoms being treated as classical. The shared proton wavefunction is to be described using a potential energy surface where the electronic structure was obtained on 51 grid points along the Cl–Cl axis using single particle, Hartree–Fock, and DFT formalisms. An illustration is provided in Fig. 1.

While these studies were performed for a large number of density matrices with varying levels of bases and density functionals, we summarize our results here by providing a representative sample. In Figs. 2 and 3, the first few singular values and singular vectors of the matrix $\mathbf{S}$ are shown. The evolution of the largest singular value with change in Cl–Cl distance is also shown in Fig. 4. For orthonormal as well as nonorthogonal atomic orbital (AO) basis sets, only a few singular values are nonzero and the number of principal
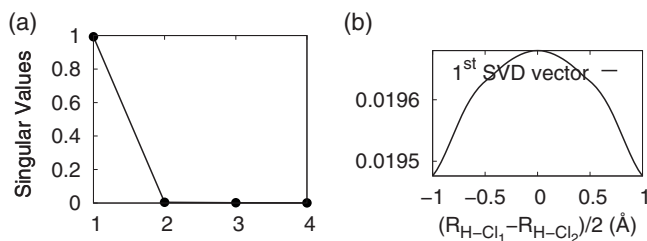
FIG. 2. (a) The first four singular value obtained using SVD analysis of the self-similarity metric matrix, Eq. (3), when the density matrices are represented in an orthonormal basis. (b) The corresponding first singular vector. The system is ClHCl^{-1} and the Cl–Cl distance has been chosen to be 3.15 Å. See Fig. 1 for definition of parameters.

FIG. 4. Evolution of the largest singular value as function of Cl–Cl distance in (a) orthonormal (b) nonorthogonal AO basis set.

components of the electronic structure that contribute at all grid points for this case are small (<4). The singular vectors represent the contributions from the original grid density matrices to the principal electronic structural components. The subtle variations in the principle components [Figs. 2(b) and 3(b)] indicate that the electronic structure can be grouped into three regions, donor/acceptor bound, and unbound contributions. More generally, it appears that the dependence of the electronic structure on the quantum nuclear grid coordinate is local. Exploiting the locality of the electronic structure is, of course, a hallmark of the TDDS function,[3,4] which uses this property to bring the number of computations down by several orders of magnitude. In this sense TDDS is connected to other nonlinear dimensionality reduction techniques[52,53] and these connections will be explored in future publications. However, the question we address in the remaining portion of this publication is whether, using such properties it would be possible to design a method where multiple single particle electronic density matrices are propagated, *each density matrix being independent of the quantum grid*, and the subtle variations of the electronic structure on the quantum grid arise when these multiple single particle density matrices are combined. This would make the resultant electronic structure at each grid point, intrinsically multireference,[54] and this multireference nature would be responsible for the variations in the dependence of electronic structure with nuclear grid.

In summary, we note that the number of principal electronic structure components needed to describe the potential surface in QWAIMD can be potentially a small number compared to the size of the quantum nuclear grid. However, one must stress an important caveat. The singular vectors determined above are linear combinations of multiple density matrices and hence the associated electronic structure is intrinsically multireference. Hence, while superficially it might appear that the problem has been simplified, the challenge reappears in a different form. To address these concerns, in the next section we present a scheme to obtain the electronic potential surface, using multiple single particle electronic density matrices. These density matrices are propagated simultaneously along with the classical nuclei and quantum wavepacket, through an extended Lagrangian formalism. The resultant surface is constructed using a nonorthogonal CI-type method.[29–36]

IV. A DIABATIC EXTENDED LAGRANGIAN FORMALISM

The high degree of self-similarity and relatively local variations of the electronic structure on the quantum nuclear grid demonstrated in the previous section is now exploited to construct a QWAIMD formalism that (a) allows the simultaneous propagation of multiple single particle electronic density matrices and (b) construction of the quantum nuclear potential surface from these multiple density matrices. To begin the discussion, we introduce the set of variables $\{R_{QM}, \mathbf{R}_C, \{\mathbf{P_i}\}\}$, where R_{QM}, as noted previously, is the quantum nuclear grid coordinate, $\mathbf{R}_C$ represents the coordinates of the classically treated nuclei and $\{\mathbf{P_i}\}$ represent a family of electronic single particle density matrices (to be treated as diabatic states) in an orthonormal basis, to be propagated and employed to construct the potential surface on the quantum nuclear grid. The wavepacket depicting the quantum nucleus, $\chi(R_{QM}; t)$ is to be propagated in time using the free-propagator in Eq. (1) along with the potential computed from the multiple electronic density matrices.

We underline, as noted in the previous section, that the individual $\mathbf{P_i}$-matrices are independent of R_{QM}. Any subtle variations of the dependence of electronic structure wavefunction on the quantum grid coordinate must arise from the multiconfigurational[54] nature due to combination of the various single particle wavefunctions arising from the individual density matrices. The electronic basis set utilized to construct the $\mathbf{P_i}$-matrices is also R_{QM}-independent and a generalized grid-based electronic basis is introduced in Sec. IV C to achieve this result. As a result of the associated limited coupling of the individual $\mathbf{P_i}$-matrices on R_{QM}, we refer to the states constructed from these density matrices as diabatic states.[55–62] In fact, as we will see later in Sec. IV B, *the only coupling retained between the density matrices and the quantized nuclear degrees of freedom is a one-electron cou-*
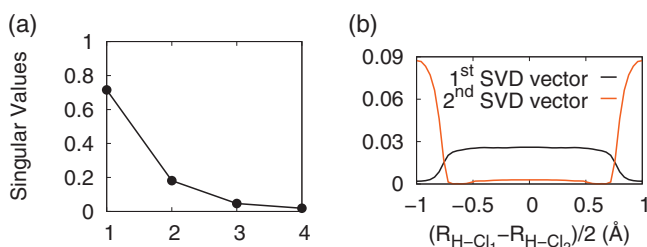

FIG. 3. (a) The first four singular values obtained from SVD analysis of the overlap matrix, Eq. (3), when the density matrices are represented in a nonorthogonal basis. (b) The corresponding singular vectors. The system is ClHCl^{-1} and the Cl–Cl distance has been chosen to be 3.15 Å. See Fig. 1 for definition of parameters.

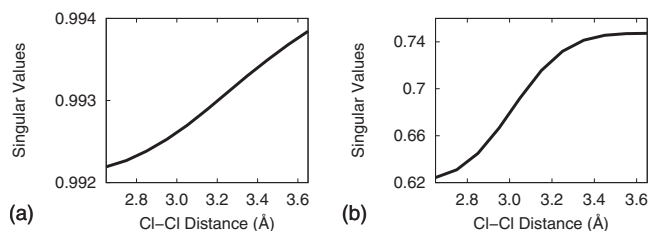*pling*. This allows for great reduction in computational effort, as will be discussed in Sec. IV B, with limited loss in accuracy, as seen in the results Sec. V B.

To represent the dynamics of the single particle density matrices and the classical nuclear framework, we introduce the diabatic extended Lagrangian,

$$\mathcal{L} = \frac{1}{2}\mathbf{Tr}[\mathbf{V}^\mathbf{T}\mathbf{MV}] + \sum_i^{N_{DM}} \frac{1}{2}\mathbf{Tr}[(\underline{\mu}_i^{1/4}\mathbf{W_i}\underline{\mu}_i^{1/4})^2]$$
$$- E(\mathbf{R_C},\{\mathbf{P_i}\},R_{QM}) - \sum_i^{N_{DM}} \mathbf{Tr}[\Lambda_i(\mathbf{P_i^2} - \mathbf{P_i})], \tag{6}$$

where $\mathbf{M}, \mathbf{V}, \mathbf{R_C}$ are the classical nuclear masses, velocity, and position, whereas $\mathbf{P_i}, \mathbf{W_i}, \underline{\mu}_i$ are the diabatic density matrix, density matrix velocity, and tensorial fictitious mass for density matrices $\mathbf{P_i}$, and N_{DM} is the number of density matrices. The multiple density matrices are coupled through the energy function, $E(\mathbf{R_C},\{\mathbf{P_i}\},R_{QM})$, which is obtained using the nonorthogonal CI-type formalism presented in Sec. IV A.

Equation (6) is an extension of the classical Lagrangian used in atom-centered density matrix propagation (ADMP),[63–66] but differs through (a) the use of multiple single particle density matrix trajectories where each density matrix has a separate *N*-representability constraint, and (b) the energy $E(\mathbf{R_C},\{\mathbf{P_i}\},R_{QM})$, which as noted depends on multiple electronic density matrices and hence *is not derived from a single particle formalism*. The form of energy and associated gradients are discussed in the next subsection.

The Euler–Lagrangian equations-of-motion for the density matrices and classical nuclei are

$$\mathbf{M}\frac{\partial^2\mathbf{R_C}}{\partial t^2} = -\langle\psi|\left.\frac{\partial E(\mathbf{R_C},\{\mathbf{P_i}\},R_{QM})}{\partial\mathbf{R_C}}\right|_{\{\mathbf{P_i}\}}|\psi\rangle, \tag{7}$$

$$\underline{\mu}_i^{1/2}\frac{\partial^2\mathbf{P_i}}{\partial t^2}\underline{\mu}_i^{1/2} = -\left[\langle\psi|\left.\frac{\partial E(\mathbf{R_C},\{\mathbf{P_i}\},R_{QM})}{\partial\mathbf{P_i}}\right|_{\{\mathbf{R_C},\mathbf{P_{j\neq i}}\}}\right.$$
$$\left. + \Lambda_i\mathbf{P_i} + \mathbf{P_i}\Lambda_i - \Lambda_i|\psi\rangle\right]. \tag{8}$$

When a single density matrix is involved, Eqs. (6)–(8) have been well studied for classical nuclear dynamics[45,65,67–72] and provide good approximations to the dynamics of a set of classical nuclei on the Born–Oppenheimer surface. It has been shown that deviations from the Born–Oppenheimer surface are bounded by variations in the fictitious kinetic energy,[64] $\mathbf{Tr}[(\underline{\mu}_i^{1/4}\mathbf{W_i}\underline{\mu}_i^{1/4})^2]$, and the commutator of the Fock and density matrices.[66]

For the current formalism involving multiple density matrices, the single particle states at the initial time-step are chosen to represent a local region of the quantum grid according to $\{\mathbf{P}_i^{\mathbf{R}_{QM}^{i^*}}(\mathbf{R_C})\}$. That is the *i*th density matrix is chosen at the initial time-step to be representative of the electronic structure around grid point $R_{QM}^{i^*}$. Thus each density matrix represents some local electronic structure on the quantum nuclear grid at the initial step. As the dynamics proceeds, these density matrices mix and the full potential surface is constructed from a CI-like description of the single

particle states obtained from these density matrices. This aspect is discussed in Secs. IV A and IV B. Hence, these density matrices, $\{\mathbf{P}_i^{\mathbf{R}_{QM}^{i^*}}(\mathbf{R_C})\}$, are akin to "valence-bond" states.[73–77] In this situation, the individual fictitious kinetic energies, $\mathbf{Tr}[(\underline{\mu}_i^{1/4}\mathbf{W_i}\underline{\mu}_i^{1/4})^2]$, represent deviations from converged diabatic representations of the electronic structure depicting the neighborhood of $R_{QM}^{i^*}$. This is similarly the case for the associated commutators of the Fock and density matrices. Furthermore, since Eq. (8) represents dynamics of $\{\mathbf{P_i}\}$ on surfaces where the commutator between the respective Fock and density matrices, $\{[\mathbf{F_i},\mathbf{P_i}]\}$ are small, we have also utilized a converged form of P_i in this publication. From hereon the dynamical formalism introduced in this section is referred to as the extended Lagrangian-QWAIMD formalism. Furthermore, when the density matrices $\mathbf{P_i}$ are converged, rather than propagated, the formalism is referred to as diabatic extended Lagrangian-QWAIMD. By contrast, the QWAIMD prescription that does not utilize an extended Lagrangian formalism, which is the formalism discussed in Refs. 1, 2, and 4–6 and is referred to in further discussion here as QWBOMD.

A. Energy expressions from the multiple, time-dependent density matrices

In this section, we construct the potential energy surface from the multiple time-dependent single particle electronic structure density matrices available from Eqs. (6) and (8). Toward this we use a nonorthogonal CI-type formalism[29–36] constructed using the Slater determinants obtained from the nonorthogonal density matrices, $\{\mathbf{P_i}\}$,

$$\begin{pmatrix} \widetilde{H}_{1,1} & \cdots & \widetilde{H}_{1,N_{DM}} \\ \vdots & \ddots & \vdots \\ \widetilde{H}_{N_{DM},1} & \cdots & \widetilde{H}_{N_{DM},N_{DM}} \end{pmatrix} \begin{pmatrix} c_1 \\ \vdots \\ c_{N_{DM}} \end{pmatrix}$$
$$= E \begin{pmatrix} 1 & \cdots & \widetilde{S}_{1,N_{DM}} \\ \vdots & \ddots & \vdots \\ \widetilde{S}_{N_{DM},1} & \cdots & 1 \end{pmatrix} \begin{pmatrix} c_1 \\ \vdots \\ c_{N_{DM}} \end{pmatrix}, \tag{9}$$

where N_{DM} is the number of density matrices in Eqs. (6) and (8). In the following discussion, we do not distinguish between the cases where the entire family of Slater determinants $\{|\Phi_i\rangle\}$ constructed from density matrices, $\{\mathbf{P_i}\}$, is a nonorthogonal set or if this set is comprised of sub-nonorthogonal sets such as $\{\cdots,\{|\Phi_{i_{M-1}}^{M-1}\rangle\},\{|\Phi_{i_M}^M\rangle\},\cdots\}$, where each subset $\{|\Phi_{i_M}^M\rangle\}$ is internally orthogonal (excited determinants). The latter would be case for an "on-the-fly" multireference CI-type description of on-the-fly dynamics. The formalism below also allows the flexibility for the multiple density matrices to signify different spin states,[78,79] if the problem necessitates such a description. The numerical benchmarks provided here, however, do not consider this situation and will be considered in future publications. We use the terminology "nonorthogonal CI-type" to encompass all of these possibilities.

The diagonal elements for the Hamiltonian in Eq. (9) are obtained using single particle energy expressions[80,81]

$$\widetilde{H}_{ii} = \langle \Phi_i | \hat{H} | \Phi_i \rangle = \mathbf{Tr}\left[\mathbf{h}\widetilde{\mathbf{P}}_{\mathbf{i}} + \tfrac{1}{2}\mathbf{G}_{\mathbf{i}}(\widetilde{\mathbf{P}}_{\mathbf{i}})\widetilde{\mathbf{P}}_{\mathbf{i}} \right] + V_{NN}, \qquad (10)$$

where $\mathbf{h}$ and $\mathbf{G_i}(\widetilde{\mathbf{P}}_{\mathbf{i}})$ are the one and two-electron matrices, V_{NN} is the nuclear repulsion energy and $\widetilde{\mathbf{P}}_{\mathbf{i}}[\equiv 3\mathbf{P}_{\mathbf{i}}^2 - 2\mathbf{P}_{\mathbf{i}}^3]$ is the McWeeny purified[49] idempotent reduced single particle density matrix represented in an orthonormal basis set, $\{\chi_l^M\}$. The electronic Hamiltonian $\hat{H}$, in an orthonormal set, $\{\chi_l^M\}$, is[82]

$$\hat{H} = \sum_{l,k} \langle \chi_l^M | h | \chi_k^M \rangle a_l^{M\dagger} a_k^M$$

$$+ \frac{1}{2} \sum_{l,k,p,q} \langle \chi_l^M \chi_k^M | \chi_p^M \chi_q^M \rangle a_l^{M\dagger} a_k^{M\dagger} a_q^M a_p^M. \qquad (11)$$

If density functional theory is utilized, $\mathbf{G_i}(\widetilde{\mathbf{P}}_{\mathbf{i}})$ includes the exchange-correlation functional. The off-diagonal elements of the Hamiltonian and overlap matrices are constructed using a SVD[30,31,33,83–86] of the matrix, s^{12},

$$s^{12} = \begin{bmatrix} \langle \chi_1^1 | \chi_1^2 \rangle & \cdots & \langle \chi_N^1 | \chi_1^2 \rangle \\ \vdots & \vdots & \vdots \\ \langle \chi_1^1 | \chi_N^2 \rangle & \cdots & \langle \chi_N^1 | \chi_N^2 \rangle \end{bmatrix}, \qquad (12)$$

which is used to define elements of the overlap matrix, $\widetilde{\mathcal{S}}$ in Eq. (9), as

$$\langle \Phi_1 | \Phi_2 \rangle = \widetilde{\mathcal{S}}_{12} = \det[s^{12}]. \qquad (13)$$

Since the Slater determinants associated with the density matrices are nonorthogonal, the individual single particle states, $\{|\chi_i^1\rangle\}$ and $|\{ \chi_i^2\rangle\}$, where the subscript denotes orbitals in two different determinants $|\Phi_1\rangle$ and $|\Phi_2\rangle$, are also nonorthogonal. In addition s^{12} is an asymmetric matrix [see Eq. (12)] and hence the SVD of s^{12} introduces a biorthogonal set of vectors,

$$|\widetilde{\chi}_i^1\rangle = \sum_k U_{ki} |\chi_k^1\rangle,$$

$$|\widetilde{\chi}_i^2\rangle = \sum_k V_{ki} |\chi_k^2\rangle, \qquad (14)$$

according to

$$\sigma_i^{12} \delta_{ij} = \langle \widetilde{\chi}_i^1 | \widetilde{\chi}_j^2 \rangle = \sum_{k,l} U_{ki}^* \langle \chi_k^1 | \chi_l^2 \rangle V_{lj} = [U^\dagger s^{12} V]_{ij}, \qquad (15)$$

where $\mathbf{U}$ and $\mathbf{V}$ are the left and right singular vectors obtained from SVD of s^{12}, with singular values $\{\sigma_i^{12}\}$. In this

biorthogonal representation, the off-diagonal overlap and Hamiltonian matrix elements are written as

$$\widetilde{\mathcal{S}}_{12} = \prod_i \sigma_i^{12} = \prod_i \langle \widetilde{\chi}_i^1 | \widetilde{\chi}_i^2 \rangle = \prod_i \sum_k \langle \widetilde{\chi}_i^1 | \chi_k^M \rangle \langle \chi_k^M | \widetilde{\chi}_i^2 \rangle, \quad (16)$$

$$\widetilde{H}_{12} = \sum_{l,k,j} \langle \chi_l^M | h | \chi_k^M \rangle \langle \widetilde{\chi}_j^1 | \chi_l^M \rangle \langle \chi_k^M | \widetilde{\chi}_j^2 \rangle \prod_{i \neq j} \sigma_i^{12}$$

$$+ \frac{1}{2} \sum_{l,k,p,q,i,j} \langle \widetilde{\chi}_i^1 | \chi_l^M \rangle \langle \widetilde{\chi}_j^1 | \chi_k^M \rangle \langle \chi_q^M | \widetilde{\chi}_j^2 \rangle$$

$$\times \langle \chi_p^M | \widetilde{\chi}_i^2 \rangle \prod_{m \neq i,j} \sigma_m^{12} [\langle \chi_l^M \chi_k^M || \chi_p^M \chi_q^M \rangle], \qquad (17)$$

$$= \sum_j \langle \widetilde{\chi}_j^1 | h | \widetilde{\chi}_j^2 \rangle \prod_{i \neq j} \sigma_i^{12} + \frac{1}{2} \sum_{i,j} \langle \widetilde{\chi}_i^1 \widetilde{\chi}_j^1 || \widetilde{\chi}_i^2 \widetilde{\chi}_j^2 \rangle \prod_{m \neq i,j} \sigma_m^{12}. \quad (18)$$

The singular value decomposition of s^{12} greatly simplifies computation of the $\widetilde{H}_{12}$, since the $\det[s^{12}]$ appears as a minor in all K^4 terms (where K is the number of basis functions) in $\widetilde{H}_{12}$. But note that the SVD is to be constructed for each pair of density matrices and hence the complexity is expected to grow quadratically with the number of density matrices. However, based on the analysis presented in Sec. III, one might expect that a few density matrices, judiciously placed on various quantum grid points would suffice. When this is true, a substantial reduction in computational complexity is demonstrated in Sec. IV B using the current formalism.

1. Effect of singularities in s^{12}

We next consider the case for singular and nonsingular s^{12} overlap matrices. For the nonsingular case, the off-diagonal elements of the Hamiltonian matrix in Eq. (18) can be written as

$$\widetilde{H}_{12} = \prod_i \sigma_i^{12} \left[\mathbf{Tr}[\mathbf{h}\widetilde{\mathbf{P}}^{12}] + \frac{1}{2}\mathbf{Tr}[\mathbf{G}(\widetilde{\mathbf{P}}^2)\widetilde{\mathbf{P}}^{12}] \right], \qquad (19)$$

where $\widetilde{\mathbf{P}}^{12}$ is the transition density matrix,[85,87]

$$\mathbf{P}_{kl}^{12} = \langle \chi_k^M | \left[\sum_j \frac{|\widetilde{\chi}_j^2\rangle\langle\widetilde{\chi}_j^1|}{\sigma_j^{12}} \right] | \chi_l^M \rangle = \sum_j \frac{\widetilde{C}_{kj}^2 \widetilde{C}_{lj}^1}{\sigma_j^{12}}. \qquad (20)$$

Here $\langle \chi_k^M | \widetilde{\chi}_j^2 \rangle = \widetilde{C}_{kj}^2$ and $\langle \widetilde{\chi}_j^1 | \chi_l^M \rangle = \widetilde{C}_{lj}^1$. When s^{12} is singular, we note that the off-diagonal elements of the Hamiltonian matrix are affected due to appearance of singular values s^{12} in Eq. (17). Depending on rank deficiency, the Hamiltonian matrix elements take the form

$$\widetilde{H}_{12} = \begin{cases} \prod_{i \neq \mu} \sigma_i^{12}[\mathbf{Tr}[\mathbf{h}\widetilde{\mathbf{Q}}^\mu] + \mathbf{Tr}[\widetilde{\mathbf{Q}}^\mu \mathbf{G}(^\mu \widetilde{\mathbf{Q}}^{12})]], & \text{if } \sigma_\mu^{12} = 0 \\[2ex] \prod_{m \neq \mu,\nu} \sigma_m^{12} \mathbf{Tr}[\widetilde{\mathbf{Q}}^\mu \mathbf{G}(\widetilde{\mathbf{Q}}^\nu)], & \text{if } \sigma_\mu^{12} = \sigma_\nu^{12} = 0 \\[2ex] 0, & \text{three or more zero singular values,} \end{cases} \qquad (21)$$

where we have introduced the density matrices,

$$(\widetilde{\mathbf{Q}}^{\mu})_{kl} = \widetilde{C}^2_{k\mu}\widetilde{C}^1_{l\mu}, \qquad (22)$$

$$(^{\mu}\widetilde{\mathbf{Q}}^{12})_{kl} = \sum_{j\neq\mu} \frac{\widetilde{C}^2_{kj}\widetilde{C}^1_{lj}}{\sigma^{12}_j}, \qquad (23)$$

$$(\widetilde{\mathbf{Q}}^{\nu})_{kl} = \widetilde{C}^2_{k\nu}\widetilde{C}^1_{l\nu}. \qquad (24)$$

The majority of computational expense is the SVD of overlap matrix s^{12} between the nonorthogonal orbitals. Thus, the total computational expense is $\mathcal{O}(N^2_{\mathrm{DM}}K^3)$, where N_{DM} is the number of density matrix trajectories. This further reduces to $\mathcal{O}(N^2_{\mathrm{DM}}K)$ when sparse matrix technology is utilized.[88–95] As stated earlier, the analysis in Sec. III indicates that N_{DM} is expected to be small as compared to the number of quantum grid points and hence the computational complexity is correspondingly reduced as noted in Sec. IV B.

In Sec. V we employ the scheme presented above, along with the generalized grid-based electronic basis functions discussed in Sec. IV C and gradients in Sec. IV D. In all calculations presented in this publication, only ground state density matrices are used. But the formalism does not present these restrictions and future publications will probe these issues further.

B. Discussion of algorithmic issues and computational advantages of xLag-QWAIMD and DxLag-QWAIMD over QWAIMD

In this section, we illustrate the computational advantage of the above formalism over traditional QWAIMD. We consider the case where the overlap matrix between orbitals, s^{12}, is full rank. (Rank deficiency does not affect the computational performance significantly.) We use the expression for the off-diagonal elements in Eq. (19) and emphasize that the coupling elements are explicit functions of the classical nuclear coordinates, $\mathbf{R_C}$, quantum nuclear grid coordinates, R_{QM}, and the transition density matrix, $\widetilde{\mathbf{P}}^{12}$. However, the key ideas that yield substantial computational gain arise from an analysis of the Hamiltonian matrix elements in Eqs. (10), (19), and (21) and are described as follows:

(a)   The diabatic nature of $\{\mathbf{P_i}\}$ allows these density matrices to be independent of R_{QM}. This essentially implies that the two-electron contributions in Eqs. (10), (19), and (21) [for example consider, $(1/2)\mathbf{Tr}[\mathbf{G}(\widetilde{\mathbf{P}}^{12})\widetilde{\mathbf{P}}^{12}]$ in Eq. (19)] are independent of R_{QM}. This is true because the two-electron integrals can be computed using orbitals used to construct $\{\widetilde{\mathbf{P}}_1\}$ [see Eqs. (19) and (21)] which are independent of R_{QM}. The independence of $\{\widetilde{\mathbf{P}}_1\}$ on R_{QM} is further facilitated by the introduction of grid-based electronic structure bases introduced in Ref. 46 and discussed in Sec. IV C. As a result, at each instant during the dynamics, only the one-electron portion is recomputed.

(b)   The potential surface at each instant for the quantum nuclear Hamiltonian is formed by keeping all classical nuclei fixed and by discretizing the quantum particle on

a set of grid points. Thus, a major portion of the one-electron electronic Hamiltonian $\mathbf{h}$ is constant at each classical time-step as well. Due to these factors, we merely need to correct the coupling element $\widetilde{H}_{12}$ across the quantum nuclear grid by calculating the one-electron part $\Delta\mathbf{h}(R_{\mathrm{QM}})$, which depends explicitly on the quantum nuclear grid points. This leads to a large reduction in computation time, as noted in Fig. 5, with negligible loss in accuracy as will be seen from the numerical results in Sec. V B.

The sequence of operations in this approach is as follows. At the first quantum mechanical grid point chosen (generally the wavepacket centroid), the full Fock matrix is computed from the propagated density matrix to provide the $\widetilde{H}_{12}$ and gradients $\partial\widetilde{H}_{12}/\partial x$ (see Sec. IV D) at that grid point. For all subsequent grid points of the same dynamics step, only the one-electron integrals which depend on R_{QM} need to be recomputed. The change in the one-electron integral between the new and the old grid point further depend only on the position of R_{QM} and this change is introduced into the old Fock matrix to obtain the new Fock matrix. This reduces the computational cost associated with obtaining the potential and gradients enormously, since computing the two-electron integrals formally scales as $\mathcal{O}(K^4/8)$ (where the factor 8 arises due to permutation symmetry) while the one-electron integral computation only scales as $\mathcal{O}(K^2)$, where K is the number of basis functions used. Note that a parallel implementation further reduces this overhead, since the effort is linear with quantum grid points. In Fig. 5, the logarithm of the total CPU time for energy and gradient evaluations on the quantum nuclear grid are compared for full-QWBOMD, TDDS-QWBOMD, DxLAG-QWAIMD, and xLAG-QWAIMD. *It can be clearly seen that DxLAG-QWAIMD and xLAG-QWAIMD are computationally advantageous by several orders of magnitude.* In our current implementation, parallelization has been exploited for full-QWBOMD and TDDS-QWBOMD. The DxLAG-QWAIMD and xLag-QWAIMD codes are currently OPENMP parallel and efforts towards an MPI implementation are ongoing. (Since Fig. 5 depicts the total CPU time, parallelization is not reflected here.)
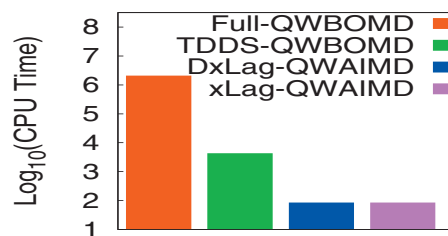

FIG. 5. The logarithm of the total CPU time for energy and gradient calculations during each QWAIMD step. The number of electronic structure calculations (energy and forces) for "full-QWBOMD," xLag-QWAIMD, and DxLag-QWAIMD is $51\times51\times101$ (size of the quantum nuclear grid). For TDDS-QWBOMD, this number has been reduced to 539 through adaptive choice of grid points according to Eq. (2). (See Refs. 3 and 4.) Only a single density matrix has been utilized for the xLag and DxLag-QWAIMD calculations.

1. Algorithmic issues for multiple density matrices including choice of density matrices at initial step

When multiple density matrices are employed, it is first necessary to construct diabatic states and associated coupling elements from individual density matrices. These may then be used to construct the adiabatic states using nonorthogonal CI. Due to the diabatic nature of the individual density matrices, there is limited (one-electron) coupling between the quantum nuclear degrees of freedom and density matrix states. To compensate for this reduced correlation between electrons and quantum nuclear degrees of freedom, multiple diabatic states were proposed in Sec. IV A. Each density matrix, as discussed in Sec. IV, includes local interactions between quantum nuclear degree of freedom and electronic structure and these are used to construct a potential surface from nonorthogonal CI. However, the choice of these diabatic states is a matter of initial conditions for dynamics. As noted in Sec. IV, the diabatic single particle states $\{\mathbf{P}_i^{\mathbf{R}_i^*}(\mathbf{R_C})\}$ are chosen such that each state represents a local electronic structure on the quantum nuclear grid at the initial step (discussed further below). Hence, these density matrices, $\{\mathbf{P}_i^{\mathbf{R}_i^*}(\mathbf{R_C})\}$, are similar to "valence-bond" states.[73–77]

The initial choice for $\{\mathbf{P}_i^{\mathbf{R}_i^*}(\mathbf{R_C})\}$ is as follows. First a set of "important" regions in the potential (a function of the quantum nuclear grid) is chosen as discussed in Ref. 46. In Ref. 46, the TDDS functions based on Shannon entropy were found to provide sufficient accuracy in probing important regions of the potential surface. Here we employ the Shannon entropy based TDDS function,

$$\omega_{\text{TDDS-Shannon}}(R_{\text{QM}}) \propto \frac{(\widetilde{S}(R_{\text{QM}}) + 1/I_S)}{(\widetilde{V}(R_{\text{QM}}) + 1/I_V)}, \qquad (25)$$

to locate significant regions of the potential. The Shannon information entropy, $S[\rho(x)] \equiv -\rho\log(\rho)$, is a function of the wavepacket density: $\rho(\mathbf{R_{QM}})$, which may be chosen based on an estimate of the ground state of a reduced dimensional potential or equivalently, $\rho(\mathbf{R_{QM}}) \equiv \Sigma_i \exp(-\beta E_i)\rho_i$. The quantity ρ_i refers to estimates of the individual eigenstates of a reduced dimensional potential surface. The quantities $\widetilde{S}$ and $\widetilde{V}$ are L^∞ normalized. These functions are shifted and scaled such that the respective values are bounded by unity.[3] The algorithm involves a Haar wavelet fit of the sampling function in Eq. (25) to obtain points in configurational space as discussed in Ref. 4. Once these significant points on the surface are computed at the initial step, the quantized degrees of freedom are placed on each of these points to compute a family of single particle electronic density matrices. This set of density matrices is then used for the propagation scheme discussed above.

In Fig. 6, the set of points obtained from such an algorithm are illustrated using vertical dashed lines. The associated diabatic states, $\widetilde{H}_{ii}(\mathbf{R_{QM}})$, computed using the density matrices, are shown in blue. These diabatic states combine with the off-diagonal elements of $\widetilde{H}$ (which are the black curves on top panel) to produce the adiabatic states provided
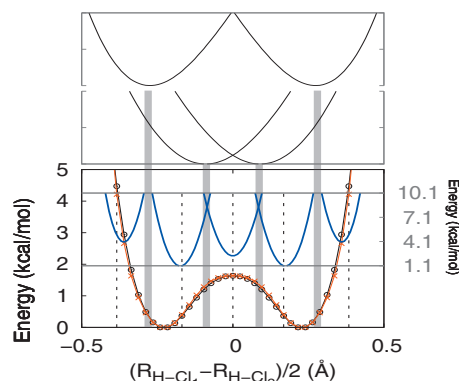

FIG. 6. An illustration for using multiple diabatic states to obtain the adiabatic potential surface. See text for details. The diabatic surfaces are seen in blue (energy axis on the right) and the resultant nonorthogonal CI surface is shown in red (energy axis on the left). The first set of off-diagonal elements is shown in the top panel. The resultant nonorthogonal CI surface (red) is in good agreement with a full potential scan (black) and a quantitative error analysis is provided in Sec. V B.

using the red and black curves at the bottom panel of Fig. 6. Specifically, the first set of off-diagonal elements of $\widetilde{H}$ that couple the diabatic states are seen in the top panel of the figure. The vertical shaded (gray) rectangles depict the couplings. That is, the leftmost shaded rectangle is positioned in between the first and second diabatic states and hence points towards the off-diagonal coupling, $\widetilde{H}_{12}$, between these diabatic states. This coupling is represented using the top-left black curve in the top panel. The second shaded rectangle (from left) is positioned between the second and third diabatic states. Hence it points toward the off-diagonal coupling in the top panel, $\widetilde{H}_{23}$, which couples second and third diabatic states, and so on. The resultant adiabatic state is obtained from the nonorthogonal CI algorithm constructed at each quantum grid point and is shown in red (scale: left vertical axis). This result is compared with a full scan surface. Clearly, the agreement is very good and a quantitative error analysis is presented in Sec. V B. The computational effort of multiple density matrices is quadratic with N_{DM} but the calculation of each coupling element is independent and hence can be performed in parallel to enhance computational scaling. It must also be noted that in constructing the red curve in the bottom panel, we have employed the ground state arising from the nonorthogonal CI formalism. The use of excited electronic states arising from this formalism will be considered in future publications.

C. Generalized, grid-based electronic basis functions that depend on the relative nuclear (R_C) positions

As illustrated in Sec. IV B, a large number of computations can be eliminated by only calculating the one-electron integral correction part to the Fock matrix arising from the quantum nuclear grid dependence. This is done through elimination of basis set dependence on R_{QM}. Instead, a set of electronic basis functions is introduced which depend on the collective classical nuclear variables, $\mathbf{R_C}$, according to

$$\chi_{l,m,n}^{\mathbf{R_F}}(\mathbf{r}) = (x - R_x)^l (y - R_y)^m (z - R_z)^n \exp[-\alpha(\mathbf{r} - \mathbf{R}_F)^2],$$
(26)

where $\mathbf{R}_F[\equiv(R_x, R_y, R_z)]$, the Gaussian center is now a function of all the classical nuclear variables according to $\mathbf{R}_F = f(\{\mathbf{R_C}\})$. This is a generalization of bond-centered basis functions[96–101] traditionally used in quantum chemistry. In this publication, since the transferring quantum proton is of primary concern, we define the Gaussian centers as function of the hydrogen bond donor and acceptor coordinates,

$$\mathbf{R}_F^i \equiv \sum_j c_{ji}\mathbf{R_C}^j + \vec{v}_i = a_i\mathbf{R_A} + d_i\mathbf{R_D} + \vec{v}_i,$$
(27)

where $\mathbf{R_A}$ and $\mathbf{R_D}$ are coordinate vectors for the donor and acceptor atoms and $\vec{v}_i$ is a uniform shift that can be used to create a three-dimensional grid of electronic basis functions. The quantities l, m, and n, in Eq. (26), are the usual orbital angular momentum indices of the basis function. In practice, the calculation can be made very accurate by placing sufficient basis functions on the chemically relevant (bonding) region. Furthermore, in a fashion similar to atom-centered basis functions, the centers of these functions also transform according to the classical nuclear positions.

In Ref. 46, these basis functions were benchmarked with respect to regular atom-centered basis functions. To arrive at a system independent choice for the grid-based basis parameters $a_i, d_i, \vec{v}_i$, the TDDS formalism was employed. Note that the parameters I_χ, $I_{V'}$, and I_V in Eq. (2) are tuned to provide an equal distribution of calculations in the classically allowed (minimum energy regions) and classically forbidden (classical turning point) regions.[3,4] The associated interpretation of $\omega_{\text{TDDS}}(R_{\text{QM}})$ is that large values of this quantity indicate regions where energy and gradient evaluations should be conducted accurately using electronic structure methods. When $\omega_{\text{TDDS}}(R_{\text{QM}})$ is small, the accuracy of energy and gradients is not critical. Similarly, utilizing the information given by TDDS in addition to other new sampling functions that use Shannon [see Ref. 47 and Eq. (25)], a flexible and accurate scheme for distributing the grid-based Gaussian basis functions was devised in Ref. 46. It was found[46] that the Shannon entropy based TDDS functions provide a very accurate description of the potential surface while eliminating the basis set dependence on the quantum nuclear degrees of freedom. Furthermore, the electronic structure calculations performed using these grid-based Gaussian basis functions are computational efficient since far fewer basis functions are found to be necessary as compared to atom-centered basis functions. These results are directly utilized in the current publication.

D. Gradients

In this section, we first derive general expressions for gradients and then provide nuclear gradients in Sec. IV D 1. The expressions for the density matrix gradients are presented in Appendices A and B. Both sets of expressions are necessary for the multireference xLAG-QWAIMD formal-

ism. But, the density matrix gradients are not necessary for the DxLAG-QWAIMD formalism since the density matrices are converged.

The eigenvalue problem in Eq. (9) can be transformed, using $\widetilde{S} = X^T X$, where X is either the Cholesky (upper triangular), Löwdin ($\widetilde{S}^{1/2}$), or SVD transformation. The associated energy expression is

$$(\mathbf{c}_i')^T \widetilde{H}' \mathbf{c}_i' = E_i,$$
(28)

where $\widetilde{H}' \equiv X^{-T}\widetilde{H}X$ and $\mathbf{c}' \equiv X\mathbf{c}$, with gradients

$$\frac{\partial E_i}{\partial x} = \frac{\partial(\mathbf{c}_i')^T}{\partial x}\widetilde{H}'\mathbf{c}_i' + (\mathbf{c}_i')^T\frac{\partial\widetilde{H}'}{\partial x}\mathbf{c}_i' + (\mathbf{c}_i')^T\widetilde{H}'\frac{\partial\mathbf{c}_i'}{\partial x},$$

$$= E_i\frac{\partial[(\mathbf{c}_i')^T\mathbf{c}_i']}{\partial x} + (\mathbf{c}_i')^T\frac{\partial\widetilde{H}'}{\partial x}\mathbf{c}_i' = (\mathbf{c}_i')^T\frac{\partial\widetilde{H}'}{\partial x}\mathbf{c}_i',$$
(29)

since $(\mathbf{c}_i')^T\mathbf{c}_i' = 1$. Using $\widetilde{H}' = X^{-T}\widetilde{H}X^{-1}$, we obtain

$$\frac{\partial E_i}{\partial x} = (\mathbf{c}_i')^T\left[\frac{\partial X^{-T}}{\partial x}\widetilde{H}X^{-1} + X^{-T}\frac{\partial\widetilde{H}}{\partial x}X^{-1} + X^{-T}\widetilde{H}\frac{\partial X^{-1}}{\partial x}\right]\mathbf{c}_i',$$

$$= (\mathbf{c}_i')^T\left[\frac{\partial X^{-T}}{\partial x}X^T\widetilde{H}' + X^{-T}\frac{\partial\widetilde{H}}{\partial x}X^{-1} + \widetilde{H}'X\frac{\partial X^{-1}}{\partial x}\right]\mathbf{c}_i',$$

$$= E_i(\mathbf{c}_i')^T\left[\frac{\partial X^{-T}}{\partial x}X^T + X\frac{\partial X^{-1}}{\partial x}\right]\mathbf{c}_i' + (\mathbf{c}_i')^TX^{-T}\frac{\partial\widetilde{H}}{\partial x}X^{-1}\mathbf{c}_i',$$

$$= -E_i(\mathbf{c}_i')^T\left[X^{-T}\frac{\partial X^T}{\partial x} + \frac{\partial X}{\partial x}X^{-1}\right]\mathbf{c}_i'$$
$$+ (\mathbf{c}_i')^TX^{-T}\frac{\partial\widetilde{H}}{\partial x}X^{-1}\mathbf{c}_i',$$

$$= -E_i(\mathbf{c}_i')^TX^{-T}\frac{\partial\widetilde{S}}{\partial x}X^{-1}\mathbf{c}_i' + (\mathbf{c'}_i)^TX^{-T}\frac{\partial\widetilde{H}}{\partial x}X^{-1}\mathbf{c}_i',$$

$$= (\mathbf{c}_i)^T\left[\frac{\partial\widetilde{H}}{\partial x} - E_i\frac{\partial\widetilde{S}}{\partial x}\right]\mathbf{c}_i,$$
(30)

where we have used the following identity:

$$X^{-T}\frac{\partial X^T}{\partial x} + \frac{\partial X}{\partial x}X^{-1} = X^{-T}\frac{\partial\widetilde{S}}{\partial x}X^{-1},$$
(31)

which can be obtained by differentiating both sides of $\widetilde{S} = X^TX$.

1. Nuclear gradients

To compute the nuclear gradients of the Hamiltonian matrix, we first note that the expressions for the diagonal elements are identical to those used in single surface ADMP.[63] Furthermore, the off-diagonal matrix elements are also identical in form to those in single surface ADMP for the case of nonsingular overlap matrix, when the density

matrix is replaced by the transition density matrix. [Compare Eqs. (10) and (19).] Thus we utilize the single surface ADMP (Ref. 63) for the diagonal elements and off-diagonal elements when the overlap matrix is nonsingular. It must be noted that the single surface ADMP gradients are more general than those standardly used in Born–Oppenheimer dynamics and optimization calculations[102] since these include

additional terms that dependent on the commutator of the Fock and density matrices and reflect the limited convergence of the density matrix within the extended Lagrangian procedure.[63,66]

The nuclear gradients for the off-diagonal Hamiltonian matrix elements for the case of singular overlap may be written as

$$
\left.\frac{\partial \widetilde{H}_{12}}{\partial \mathbf{R}_C}\right|_{\{\mathbf{P}_i\}} =
\begin{cases}
\prod\limits_{i \neq \mu} \sigma_i^{12} \left[\mathbf{Tr}\left[\left.\frac{\partial \mathbf{h}}{\partial \mathbf{R}_C}\right|_{\{\mathbf{P}_i\}} \widetilde{\mathbf{Q}}^\mu \right] + \mathbf{Tr}\left[\widetilde{\mathbf{Q}}^\mu \left.\frac{\partial \mathbf{G}(^\mu \widetilde{\mathbf{Q}}^{12})}{\partial \mathbf{R}_C}\right|_{\{\mathbf{P}_i\}} \right] \right], & \text{if } \sigma_\mu^{12} = 0 \\[2ex]
\prod\limits_{m \neq \mu, \nu} \sigma_m^{12} \, \mathbf{Tr}\left[\widetilde{\mathbf{Q}}^\mu \left.\frac{\partial \mathbf{G}(\widetilde{\mathbf{Q}}^\nu)}{\partial \mathbf{R}_C}\right|_{\{\mathbf{P_i}\}} \right], & \text{if } \sigma_\mu^{12} = 0 \quad \text{and} \quad \sigma_\nu^{12} = 0 \\[2ex]
0, & \text{if } \#\{\sigma_\mu^{12} = 0\} \geq 3,
\end{cases}
\tag{32}
$$

It must be noted that the gradients of the one-electron and two-electron terms, $\partial \mathbf{h}/\partial \mathbf{R}_C|_{\{\mathbf{P}_i\}}$ and $\partial \mathbf{G}/\partial \mathbf{R}_C|_{\{\mathbf{P}_i\}}$, above are presented in the orthonormal basis. When transformed to the nonorthogonal representation, additional terms including derivatives of the transformation matrices (Löwdin or Cholesky) arise as discussed in Refs. 63 and 66. These additional terms are included in our calculations.

V. NUMERICAL TESTS

This section is organized as follows. The single diabatic state DxLag-QWAIMD and xLag-QWAIMD dynamics calculations performed using grid-based basis functions are discussed in Sec. V A. Particular attention is directed in Sec. V A toward energy conservation properties of the simulation

algorithm. The effect of using multiple density matrices on the accuracy of the shared proton potential surface is discussed in Sec. V B. In Sec. V C, we present an analysis of the DxLag-QWAIMD dynamics when multiple diabatic states are used. Specifically, vibrational properties are contrasted between the single and multiple density matrix cases.

A. Dynamics using xLag-QWAIMD and DxLag-QWAIMD: Single diabatic surface

In this section we analyze the energy conservation and dynamical properties of the xLag-QWAIMD and DxLag-QWAIMD algorithms. [Note that while xLag-QWAIMD involves the quantum dynamical evolution of the shared proton along with the extended Lagrangian dynamics of the classi-

TABLE I. Analysis of energy conservation and computational effort for xLag-QWAIMD and DxLag-QWAIMD. Single diabatic state, NVE ensemble.

Methods[a]		Grid basis, quantum/classical[b]	Temp.[c] (K)	Simulation time (ps)	ΔE [d]	Quantum grid dimension	Number of grid points[e]	CPU time[f] (s)
DxLag[g]	HF	STO-3G/6-31+G**	551.1	2.2	0.008	1D	101	9.48
xLag[h]	HF	STO-3G/6-31+G**	530.2	1.6	0.064	1D	101	9.48
QWBOMD	HF	STO-3G/6-31+G**	417.6	1.7	0.052	1D	101	871.93
DxLag[e]	HF	STO-3G/6-31+G**	1553.2	0.9	0.044	3D	262 701	84.56
xLag[g]	HF	STO-3G/6-31+G**	1421.6	1.2	0.855	3D	262 701	84.56
DxLag[e]	HF	STO-3G/aug-cc-pvtz	1544.9	1.1	0.074	3D	262 701	326.15
xLag[g]	HF	STO-3G/aug-cc-pvtz	1413.7	0.4	0.035	3D	262 701	321.40
DxLag[e]	B3LYP[i]	STO-3G/6-31+G**	1699.0	1.2	0.014	3D	262 701	253.48
xLag[g]	B3LYP	STO-3G/6-31+G**	1552.2	0.6	0.456	3D	262 701	163.43
DxLag[e]	B3LYP	STO-3G/aug-cc-pvtz	1688.3	0.6	0.057	3D	262 701	585.32
xLag[g]	B3LYP	STO-3G/aug-cc-pvtz	1539.9	0.3	0.066	3D	262 701	409.42

[a]In this column, HF implies Hartree–Fock. When DFT is used the functional is B3LYP.
[b]Refers to the fact that the grid-based basis is STO-3G and the atom-centered basis on the classical atoms is either 6-31+G** or aug-cc-pvtz.
[c]Computed using $E_{kinetic} = (3/2)nkT$, where n denotes the number of atoms and k denotes the Boltzmann constant.
[d]rms deviation of total energy (kcal/mol).
[e]For 1D: 101 grid points along the Cl–Cl axis. For 3D: 101 grid points along the Cl–Cl axis and 51 along orthogonal directions.
[f]Total CPU time for energy and gradients evaluations.
[g]DxLag: time-step for classical nuclei 0.25 and 0.05 fs for quantum propagation in all DxLag calculations.
[h]xLag: time-step for classical nuclei 0.1 and 0.02 fs for quantum propagation in all DxLag calculations. Fictitious mass is $\approx$180 a.u. in all xLag calculations.
[i]Ultrafine exchange-correlation quadrature grid (99,590) (Refs. 115–118).

cal nuclei and electronic structure, as given by Eqs. (7) and (8), the DxLag-QWAIMD algorithm, differs through the use of converged density matrices as discussed in the paragraph following Eq. (8).] The system studied here is [ClHCl]$^-$. This has been the subject of many experimental and theoretical studies[42,103–109] and contains a shared proton undergoing excursions between donor-acceptor moieties. It has also been seen in previous studies that the system presents a challenge on account of significant electron-nuclear coupling.[4,42] Furthermore, the stable triatomic configuration represents a high-interaction region between the constituent atoms presenting a significant challenge to perturbative treatments using Jacobi coordinates.[110–113] Our goal here is to gauge the accuracy and efficiency of the xLag-QWAIMD and DxLag-QWAIMD frameworks. All calculations in this publication are performed using a development version of the Gaussian series[114] of electronic structure codes.

We utilize the grid-based electronic basis functions specified in Sec. IV C. These grid-based basis functions have been well benchmarked in Ref. 46. We further note that in practical calculations, although numerical techniques such as SVD can be employed to eliminate basis set linear dependency, it is preferable to perform calculations using basis sets where the linear dependency is small. This is especially important for xLag-QWAIMD, since elimination of linear dependent basis functions results in a change in the size of the propagated density matrix. To avoid linear dependency of basis set in xLag-QWAIMD, we have found that grid-based basis functions with, $a_i = d_i = 0.5$ and spacing $|\vec{v}_i| \approx 0.2$ Å [see Eq. (27)] lead to sufficiently high accuracy. In addition split valence bases, 6-31+G** and aug-cc-pvtz, were employed on the two chlorine atoms all through dynamics. Details of simulations are summarized in Table I.

Firstly, it is important to note that the total energy and angular momentum are well conserved in all trajectories. For the xLag-QWAIMD method, fictitious kinetic energy is maintained to be two orders of magnitude smaller than the nuclear kinetic energy in these NVE simulations. This provides the expected separation between the electronic and nuclear degrees of freedom and hence conserves diabaticity.[64,66] However, the conservation properties for DxLag-QWAIMD are an order of magnitude superior to that in xLag-QWAIMD. This when coupled with the fact that the time-steps used during the DxLag-QWAIMD simulations are larger than those for the xLag-QWAIMD indicate that the former is the preferred approach for larger sized systems. Furthermore, there is an insignificant difference in computational effort between the xLag-QWAIMD and DxLag-QWAIMD formalisms as noted from Table I and Fig. 5.

To benchmark the accuracy of xLag-QWAIMD and DxLag-QWAIMD, we compare the results obtained from these simulations with a one-dimensional QWBOMD simulation, where the potential surface is obtained from converged SCF calculations on all 1D grid points. Differences in the potential energy between xLag-QWAIMD, DxLag-QWAIMD, and QWBOMD are shown in Fig. 7(a) and the corresponding motion of the wavepacket centroid is shown in Fig. 7(b). The Cl–Cl oscillation time-scales are shown in Fig. 7(c). As noted earlier, these calculations are performed using a single diabatic surface. In Sec. V C, the results obtained here are compared with those from DxLag-QWAIMD trajectories using multiple diabatic states. While the potential energies from xLag-QWAIMD and DxLag-QWAIMD are in close agreement, they differ from that obtained in QWBOMD. The discrepancy is the result of the fact that only a single diabatic density matrix has been used in these calculations and underlines the need for multiple density matrices within xLag-QWAIMD and DxLag-QWAIMD formalisms.

TABLE II. Nonorthogonal CI error analysis using five density matrices.

System	Donor-acceptor distance (Å)	Grid basis, quantum/classical[a]	Error in PES[b] ΔV[c]	Error in PES[b] ΔV[d]	Barrier height (kcal/mol)
[ClHCl]$^{-1}$	3.05	STO-3G/6-31+G**	0.05	0.75	e
	3.13	STO-3G/6-31+G**	0.04	0.28	0.34
	3.23	STO-3G/6-31+G**	0.05	0.48	1.64
	3.33	STO-3G/6-31+G**	0.17	1.94	3.79
[H$_3$O$_2$]$^{-1}$	2.40	STO-3G/6-31+G**	0.01	0.21	0.23
	2.48	STO-3G/6-31+G**	0.03	0.92	1.46
	2.58	STO-3G/6-31+G**	0.19	1.86	4.10
	2.68	STO-3G/6-31+G**	0.51	f	7.87
[H$_5$O$_2$]$^{-1}$	2.39	STO-3G/6-31+G**	0.01	0.23	g
	2.49	STO-3G/6-31+G**	0.01	0.71	0.66
	2.59	STO-3G/6-31+G**	0.07	2.73	2.69

[a]Refers to the fact that the grid-based basis is STO-3G and the atom-centered basis on the classical atoms is either 6-31+G**.
[b]Errors (in kcal/mol) computed using Eq. (33) between full-QWBOMD and nonorthogonal CI utilizing five multiple diabatic states.
[c]Range is chosen as $\epsilon_1 = 0.0$, $\epsilon_2 = E_{barrier}$, where $E_{barrier}$ is the barrier height given by the last column. See Eq. (33).
[d]Range is chosen as $\epsilon_1 = E_{barrier}$, $\epsilon_2 = 15.0$, where $E_{barrier}$ is the barrier height given by the last column. See Eq. (33).
[e]Single well potential. Ranges for comparison are chosen as the same as Cl–Cl distance of 3.13 Å.
[f]Region not sampled under the temperature conditions chosen for dynamics.
[g]Single well potential. Ranges for comparison are chosen as the same as oxygen-oxygen distance of 2.49 Å.

In the next section we benchmark the accuracy of nonorthogonal CI based method in reproducing the potential surface correctly when multiple density matrices are employed, before embarking into a benchmark on multiple density matrix propagation in Sec. V C.

B. Analysis of energy surfaces obtained from the nonorthogonal CI formalism

In this section we evaluate the accuracy of the potential surface when multiple density matrices are utilized within the xLag-QWAIMD and DxLag-QWAIMD formalisms. Our test case involves three well studied ion clusters:[42,67,68,103,107,108,119–125] the bihalide cluster $[ClHCl]^{-1}$, the hydroxide water cluster $[OH-H_2O]^{-1}$, and the Zundel cation $[H_2O-H-H_2O]^+$. Potential surfaces utilizing multiple density matrices through the nonorthogonal CI formalism are obtained for each cluster at different hydrogen bond donor-acceptor distances. While a detailed examination of the accuracy of the associated potential surface has been conducted, a few representative samples are provided here. The surfaces obtained from the xLag-QWAIMD, nonorthogonal CI formalism presented above are compared to those obtained from a full scan of the potential surface obtained using converged wavefunctions as performed in QWBOMD. To quantify numerical error, we define

$$\Delta V(\epsilon_1, \epsilon_2) = \sqrt{\frac{\sum_i [V_1(\mathbf{R_C}, \mathbf{R_{QM}^i}) - V_2(\mathbf{R_C}, \mathbf{R_{QM}^i})]^2 \Pi_{\epsilon_1, \epsilon_2}(V(\mathbf{R_{QM}^i}))}{\sum_i \Pi_{\epsilon_1, \epsilon_2}(V(\mathbf{R_{QM}^i}))}}, \tag{33}$$

where the boxcar function is defined as linear combination of Heaviside functions, $\Pi_{\epsilon_1, \epsilon_2}(V) = H(V - \epsilon_1) - H(V - \epsilon_2)$. Equation (33) allows us to inspect the accuracy in the potential surface in a tiered fashion by focusing on specific energy domains.

The algorithm used to obtain the potential surfaces is described in Sec. IV B 1. The valence-bond regions are chosen as per Eq. (25) and diabatic surfaces and coupling elements are constructed. The associated CI matrix is then diagonalized at each grid point to obtain the adiabatic surface. (See Fig. 6 and associated discussion in Sec. IV B 1 for an illustration of the algorithm.) While in principle any of the adiabatic surfaces (ground or excited) could be chosen, in this publication we have only benchmarked the ground state surfaces. Specifically, the energy surface is constructed using five diabatic states through the nonorthogonal CI specification in Sec. IV A and compared with surfaces obtained from full-QWBOMD. A detailed error analysis is presented in Table II and surfaces obtained from both methods are shown in Figs. 8–10. The figures present the energy surface constructed using five diabatic states through the nonorthogonal CI formalism. The resultant energy surfaces are numerically accurate over a range of donor-acceptor distances as noted in Table II.

C. Dynamical DxLag-QWAIMD studies using multiple diabatic single particle density matrix states

In this section, we present preliminary results of DxLag-QWAIMD by utilizing multiple diabatic states. The system studied here is $[ClHCl]^{-1}$. In Sec. V A, it was shown that although reasonable energy conservation was obtained in both xLag-QWAIMD and DxLag-QWAIMD simulations, the dynamical results differed from those in QWBOMD. See, for example, the evolution of potential and ClCl distance in Fig. 7. Since these diabatic states are defined as having minimal coupling with the quantum nuclear degrees of freedom, the resultant single diabatic surface is highly confining leading to the results seen in Fig. 7. Here, we utilize multiple diabatic states to compute a DxLag-QWAIMD trajectory. The number of diabatic states chosen here is influenced by the fact that five diabatic states provided reasonable accuracy in computing the energy surfaces given in the previous section. As a result, to study the behavior of the algorithm with number of diabatic states, in this section we include results obtained from five, seven, and nine states. The initial positions of these diabatic states are determined using the Shannon entropy based TDDS as discussed in Sec. IV B. To make direct comparison, the initial conditions in our multiple diabatic states DxLag-QWAIMD trajectory are adjusted to be identical to those in a referenced QWBOMD trajectory. The resultant trajectory again conserves energy well, with fluctuations in total energy of the order of few-tenths kcal/mol over about picosecond length simulation time. We further note that both the classical and quantum time-step in these multisurface DxLag-QWAIMD trajectories can be as large as 0.5 and 0.1 fs, respectively, without significant loss in total energy conservation. This indicates that the multisurface DxLag-QWAIMD trajectories are stable in terms of finite step numerical integration.
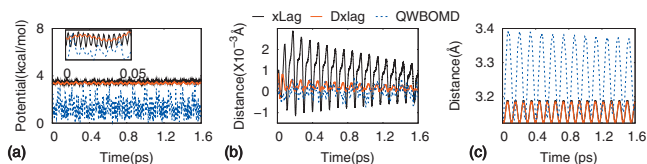

FIG. 7. Evolution of (a) averaged potential (b) wavepacket centroid in the center-of-mass frame (c) Cl–Cl distance during xLag and DxLag-QWAIMD and QWBOMD trajectory calculations. Note that a shorter time range of [0,0.05] ps for averaged potential is shown in the inset in (a). In the Cl–Cl distance plot, xLag and DxLag results coincide with each other.

To probe the resultant vibrational properties, we calculate the density of states for the classical motions (Cl–Cl stretch) by evaluating the Fourier transform of velocity autocorrelation function (FT-VAC):[45,67,71,72]

$$I_V(\omega) = \lim_{T \to \infty} \int_{t=0}^{t=T} dt \, \exp(-\iota \omega t) \langle \tilde{\mathbf{V}}(0) \cdot \tilde{\mathbf{V}}(t) \rangle. \quad (34)$$

It has been shown in Ref. 4 that spectral results from three-dimensional QWBOMD simulations, obtained using the expression above, reproduce the motion of the heavy atoms well and in good agreement with the velocity modulation spectroscopy results obtained by Kawaguchi and co-workers.[103] In the current study we compare the DxLag-QWAIMD spectral results with those from one-dimensional QWBOMD to ascertain the validity of the proposed methodology in reproducing results from the more expensive QWBOMD formalism, at cheaper computation cost. Future studies will be directed towards direct comparison with experiment. The FT-VAC from fully converged QWBOMD and DxLag-QWAIMD trajectories are presented in Fig. 11(a). We note that the single diabatic state trajectory provides a poor approximation to Cl–Cl vibrations. The multiple diabatic state approximation drastically improves on this result due to better performance in modeling the dynamical potential surface that is experienced by the quantized nuclear degrees of freedom as seen in the previous section. Furthermore, there appears a monotonic improvement of Dx-Lag-QWAIMD results tending towards the more expensive QWBOMD results, as the number of diabatic states is increased. [See Fig. 11(a).]

To further quantify the errors in multisurface DxLag-QWAIMD, an error estimate of the difference in wavepacket density, defined as

$$\Delta \rho(t) = \int dx [\rho_{\text{DxLag-QWAIMD}}(x;t) - \rho_{\text{QWBOMD}}(x;t)], \quad (35)$$

is provided in Fig. 12(a). This allows direct inspection of wavepacket density between the two trajectories over grid and over time. Clearly the errors are small. In summary we note that the multisurface DxLag-QWAIMD formalism provides results in reasonable agreement with QWBOMD with much improved computational performance.

VI. CONCLUSION

In this study, we present a new scheme which generalizes our quantum wavepacket *ab initio* molecular dynamics using nonorthogonal multireference single particle electronic density matrices within a diabatic extended Lagrangian formalism. Triggered by a principal component analysis of the electronic structure on a quantum grid, we arrive at the fact that localized diabatic states can be propagated using a modified extended Lagrangian scheme, in a coupled, concerted fashion. The propagation scheme for the electronic structure is obtained when the diabatic electronic states are mapped onto a set of classical parametric variables and subsequently propagated simultaneously with the quantum wavepacket and classical nuclei. The potential energy surface for the quantum propagation is constructed from these diabatic states using an intrinsically multiconfigurational nonorthogonal CI representation. Computational gains arise by adopting generalized grid-based electronic basis functions to account for the electronic structure in the bonding region, where the basis function centers are collective variables that depend on all classically treated nuclei. The judicious placement of basis functions arises from a novel sampling function that is tempered through the use of Shannon entropy. Essentially, the sampling function yields a compact and efficient distribution of electronic basis functions, where both numerical accuracy and stability are achieved compared to large atom-centered basis set results. Such grid-based electronic basis functions eliminate the basis set dependence on the quantum nucleus thus reinforcing the diabatic nature of the density matrices used in the proposed generalizations to QWAIMD. In fact, the diabatic nature of these density matrices modulates the coupling between the quantum nuclear degrees of freedom and the density matrix states. In this case the coupling is reduced to one that only includes single particle interactions between the electronic and quantum nuclear degrees of freedom. Further correlation, of course, arises when these single particle density matrix states are combined through the nonorthogonal CI procedure. Thus, by reusing two-electron integrals during the on-the-fly potential energy surface computation stage, we note that the computational costs can be substantially reduced. Specifically, the methods derived here turns out to be about two orders of magnitude faster than our previous developed time-dependent deterministic sampling implementation of QWAIMD.

The dynamical trajectory calculations are stable. Accuracy is probed through computation of potential surfaces for several hydrogen bonded clusters. Furthermore, vibrational properties are also computed and found to be reproduced by the new formulations at a fraction of computational cost.

APPENDIX A: DENSITY MATRIX GRADIENTS

The density matrix gradients are essential for the xLag-QWAIMD formalism but are not required for the DxLag-QWAIMD formalism. The associated forms for the diagonal elements of the Hamiltonian are identical to those in single surface ADMP and are written using the McWeeny purification,[49] $\mathbf{P}_i^{\mathbf{Mc}} = 3\mathbf{P}_i^2 - 2\mathbf{P}_i^3$, as
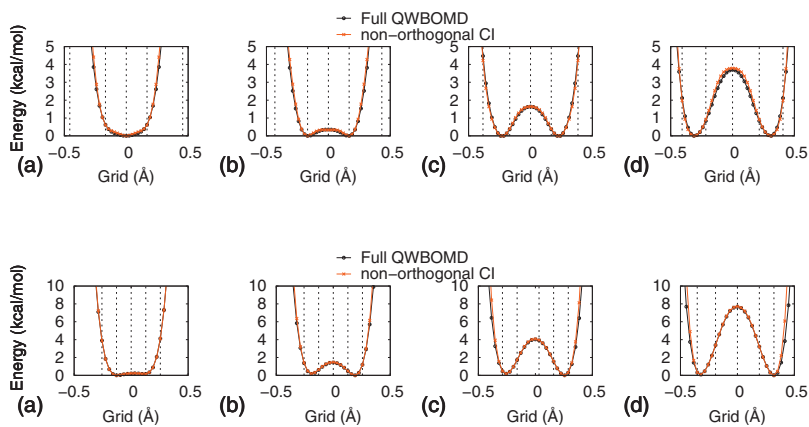
FIG. 8. Energy surface constructed using five diabatic states through nonorthogonal CI as specified Sec. IV A is compared with the surface from full-QWBOMD for $[ClHCl]^{-1}$ at Cl–Cl distance (a) 3.05, (b) 3.13, (c) 3.23, and (d) 3.33 Å. The vertical dashed lines represent the locations for diabatic state $\{P_i(R_{QM})\}$, determined using the Shannon entropy form of TDDS, Eq. (25).

FIG. 9. Energy surface constructed using five diabatic states through nonorthogonal CI as specified Sec. IV A is compared with the surface from full-QWBOMD for $[H_3O_2]^{-1}$ at oxygen-oxygen distance (a) 2.40, (b) 2.48, (c) 2.58, and (d) 2.68 Å. The vertical dashed lines represent the locations for diabatic state $\{P_i(R_{QM})\}$, determined using the Shannon entropy form of TDDS, Eq. (25).

$$\left. \frac{\partial H_{ii}}{\partial \mathbf{P_i}} \right|_{\{R_C, P_{j \neq i}\}} = 3F_iP_i + 3P_iF_i - 2F_iP_i^2 - 2P_iF_iP_i$$
$$- 2P_i^2F_i. \tag{A1}$$

The gradients for the off-diagonal elements of the Hamiltonian and overlap are complicated since these are not pure functions of $\{P_i\}$. (See Eqs. (16), (19), and (21).) These can, however, be written in terms of MO coefficients as

$$\frac{\partial \widetilde{H}_{12}}{\partial \mathbf{P}_1^{\alpha\beta}} = \sum_{\gamma\tau} \frac{\partial \widetilde{H}_{12}}{\partial \widetilde{C}_{\gamma\tau}^1} \frac{\partial \widetilde{C}_{\gamma\tau}^1}{\partial \mathbf{P}_1^{\alpha\beta}}, \tag{A2}$$

where $\widetilde{C}_{\gamma\tau}^1$ are the SVD basis vectors defined in Eq. (20) and $\partial \widetilde{H}_{12}/\partial \widetilde{C}_{\gamma\tau}^1$ can be obtained from Eq. (17). To simplify the discussion, we present the (1,2)th elements of the diabatic Hamiltonian and all other cases are similar. Additionally, we have dropped the symbol $\{|_{\{R_C, P_{j \neq i}\}}\}$ all through for notational convenience. Since the $\widetilde{C}^1$ are eigenstates of P_1, i.e., $P_1\widetilde{C}^1 = \widetilde{C}^1$, we obtain

$$\sum_k \left[\frac{\partial \mathbf{P}_1^{jk}}{\partial \mathbf{P}_1^{\gamma\tau}} \widetilde{C}_{kl}^1 + \mathbf{P}_1^{jk} \frac{\partial \widetilde{C}_{kl}^1}{\partial \mathbf{P}_1^{\gamma\tau}} \right] = \frac{\partial \widetilde{C}_{jl}^1}{\partial \mathbf{P}_1^{\gamma\tau}}, \tag{A3}$$

or

$$\frac{\partial \widetilde{C}_{jl}^1}{\partial \mathbf{P}_1^{\gamma\tau}} - \sum_k \mathbf{P}_1^{jk} \frac{\partial \widetilde{C}_{kl}^1}{\partial \mathbf{P}_1^{\gamma\tau}} = \delta_{j\gamma} \widetilde{C}_{\tau l}^1. \tag{A4}$$

These equations define a set of linear equations for the rank-4 tensor $\{\partial \widetilde{C}_{jl}^1/\partial \mathbf{P}_1^{\gamma\tau}\}$ and are solved by inverting the rank-8 tensor with elements
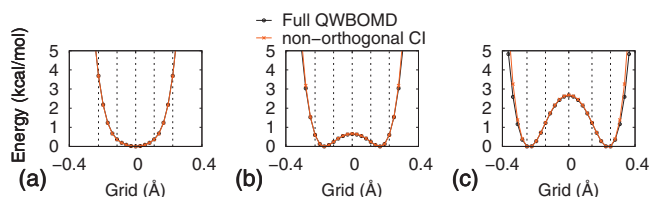

FIG. 10. Energy surface constructed using five diabatic states through nonorthogonal CI as specified in Sec. IV A compared with that of full-QWBOMD for $[H_5O_2]^{-1}$ at oxygen-oxygen distance (a) 2.39, (b) 2.49, and (c) 2.59 Å. The vertical dashed lines represent the locations for diabatic state $\{P_i(R_{QM})\}$, determined using the Shannon entropy form of TDDS, Eq. (25).

$$[\delta_{jj'} - \mathbf{P}_1^{jj'}]\delta_{ll'}\delta_{\gamma\gamma'}\delta_{\tau\tau'}, \tag{A5}$$

to obtain

$$\delta_{\tau\tau'}\delta_{\gamma\gamma'}\delta_{ll'}[\delta_{jj'} - \mathbf{P}_1^{jj'}]^{-1}. \tag{A6}$$

The inverse above acts on the rank-4 tensor, $\delta_{j\gamma}\widetilde{C}_{\tau l}^1$, where all indices are summed over, leading to an expression for $\{\partial \widetilde{C}_{jl}^1/\partial \mathbf{P}_1^{\gamma\tau}\}$. Note that the generalized inverse (density matrix P_1 is singular) in Eq. (A6) can be performed by utilizing the eigenstates of P_1. Some comments are in order with respect to the structure of density matrix gradients. In Eq. (A4), the right hand side is comprised of the occupied orbitals whereas the left-hand side consists of virtual orbitals (in the form $I - P_1$), hence, the density matrix gradients involve occupied-virtual block mixing inside each $\{P_i; I - P_i\}$ space (which may be different for different quantum grid points). Furthermore, different diabatic density matrices are coupled with each other through the off-diagonal terms $\partial \widetilde{H}_{12}/\partial \widetilde{C}_{\gamma\tau}^1$ as specified in Eq. (A2).

With regards to the overlap derivatives, from Eq. (16), we obtain

$$\frac{\partial \widetilde{S}_{12}}{\partial \widetilde{C}_{\gamma\tau}^1} = \widetilde{C}_{\gamma\tau}^2 \prod_{i \neq \tau} \sigma_i^{12}. \tag{A7}$$

To facilitate the discussion for gradients of off-diagonal elements with respect to MO coefficients $\partial \widetilde{H}_{12}/\partial \widetilde{C}_{\gamma\tau}^1$ as specified in Eq. (A2), we also write out derivatives of terms similar to the overlap $\widetilde{S}$ in Eq. (A7) as

$$\frac{\partial \left[\prod_{i \neq j} \sigma_i^{12} \right]}{\partial \widetilde{C}_{\gamma\tau}^1} = \widetilde{C}_{\gamma\tau}^2 \prod_{\substack{i \neq j, \tau \\ \tau \neq j}} \sigma_i^{12}, \tag{A8}$$

$$\frac{\partial \left[\prod_{m \neq i,j} \sigma_m^{12} \right]}{\partial \widetilde{C}_{\gamma\tau}^1} = \widetilde{C}_{\gamma\tau}^2 \prod_{\substack{m \neq i,j,\tau \\ \tau \neq i,j}} \sigma_m^{12}, \tag{A9}$$

where both terms appear in the expression for off-diagonal elements as in Eq. (17).

Using expression in Eq. (A7), the density matrix gradients of the overlap $\widetilde{S}$ can be written as
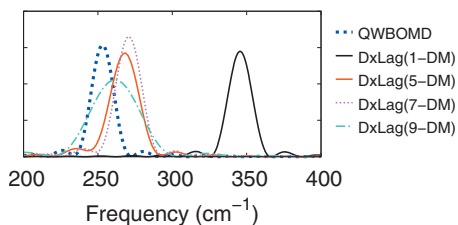
FIG. 11. Comparison of FT-VAC, Eq. (34), for the classical chloride atoms in the multistate DxLag-QWAIMD trajectories, full-QWBOMD, and single diabatic surface DxLag-QWAIMD. It is clear that the multistate DxLag-QWAIMD vibrational structure approaches the full-QWBOMD result.

FIG. 12. Evolution of wavepacket density difference $\Delta\rho$ as defined in Eq. (35) between multistate DxLag-QWAIMD and full-QWBOMD. The simulation uses five density matrices.

$$\frac{\partial \widetilde{S}_{12}}{\partial \mathbf{P}_1^{\alpha\beta}} = \sum_{\gamma\tau} \frac{\partial \widetilde{S}_{12}}{\partial \widetilde{C}_{\gamma\tau}^1} \frac{\partial \widetilde{C}_{\gamma\tau}^1}{\partial \mathbf{P}_1^{\alpha\beta}} = \sum_{\gamma\tau} \widetilde{C}_{\gamma\tau}^2 \prod_{i\neq\tau} \sigma_i^{12} \frac{\partial \widetilde{C}_{\gamma\tau}^1}{\partial \mathbf{P}_1^{\alpha\beta}}. \quad (A10)$$

We can conveniently write the above equation in matrix form as

$$\frac{\partial \widetilde{S}_{12}}{\partial \mathbf{P}_1^{\alpha\beta}} = \begin{cases} \widetilde{S}_{12} \, \mathbf{Tr}[(\bar{\mathbf{C}}^2)^{\mathbf{T}} \mathbf{D}^{\alpha\beta}], & \text{if } \#\{\sigma_\mu^{12}=0\}=0 \\ \prod_{i\neq\mu} \sigma_i^{12} \, \mathbf{Tr}[\bar{\mathbf{C}}_\mu^2 (\bar{\mathbf{C}}_\mu^2)^{\mathbf{T}} \mathbf{D}_\mu^{\alpha\beta}], & \text{if } \sigma_\mu^{12}=0 \\ 0, & \text{if } \#\{\sigma_\mu^{12}=0\}\geq 3, \end{cases} \quad (A11)$$

where

$$\bar{\mathbf{C}}_{\gamma\tau}^2 = \frac{\widetilde{C}_{\gamma\tau}^2}{\sigma_\tau^{12}},$$

$$(\bar{\mathbf{C}}_\mu^2)_\gamma = \bar{\mathbf{C}}_{\gamma\mu}^2,$$

$$\mathbf{D}_{\gamma\tau}^{\alpha\beta} = \frac{\partial \widetilde{C}_{\gamma\tau}}{\partial \mathbf{P}_1^{\alpha\beta}},$$

$$(\mathbf{D}_\mu^{\alpha\beta})_\gamma = \mathbf{D}_{\gamma\mu}^{\alpha\beta}. \quad (A12)$$

For density matrix gradient of off-diagonal elements, we only write the expression for the case where all the singular values of the orbital overlap matrix s^{12} are nonzero, all the other cases can be found 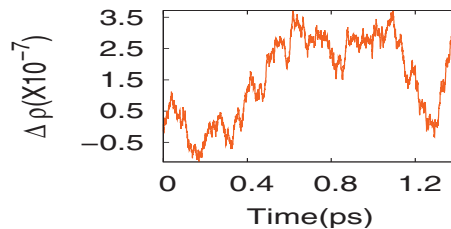in Appendix B. From Eq. (17), we can write down the expression for $\partial \widetilde{H}_{12}/\partial \widetilde{C}_{\gamma\tau}^1$ as

$$\frac{\partial \widetilde{H}_{12}}{\partial \widetilde{C}_{\gamma\tau}^1} = \sum_k h_{\gamma k} \widetilde{C}_{k\tau}^2 \prod_{i\neq\tau} \sigma_i^{12} + \sum_{kpqj} \widetilde{C}_{kj}^1 \widetilde{C}_{qj}^2 \widetilde{C}_{p\tau}^2 \prod_{m\neq\tau,j} \sigma_m^{12} \langle \gamma k || pq \rangle$$

$$+ \sum_{lkj} h_{lk} \widetilde{C}_{lj}^1 \widetilde{C}_{kj}^2 \widetilde{C}_{\gamma\tau}^2 \prod_{\substack{i\neq j,\tau \\ \tau\neq j}} \sigma_i^{12}$$

$$+ \frac{1}{2} \sum_{lkpqij} \widetilde{C}_{li}^1 \widetilde{C}_{kj}^1 \widetilde{C}_{qj}^2 \widetilde{C}_{pi}^2 \langle lk || pq \rangle \widetilde{C}_{\gamma\tau}^2 \prod_{\substack{m\neq i,j,\tau \\ \tau\neq i,j}} \sigma_m^{12}, \quad (A13)$$

where the last two terms come from Eqs. (A8). Note that the summation over τ is constrained in the last two terms. Hence, we can write down the expression for density matrix gradient for off-diagonal elements as

$$\frac{\partial \widetilde{H}_{12}}{\partial \mathbf{P}_1^{\alpha\beta}} = \widetilde{S}_{12} \left[\sum_{\gamma\tau k} h_{\gamma k} \frac{\widetilde{C}_{k\tau}^2}{\sigma_\tau^{12}} + \sum_{\gamma\tau kpqj} \frac{\widetilde{C}_{kj}^1 \widetilde{C}_{qj}^2 \widetilde{C}_{p\tau}^2 \langle \gamma k || pq \rangle}{\sigma_j^{12} \sigma_\tau^{12}} \right.$$

$$+ \sum_{\substack{\gamma\tau lkj \\ \tau\neq j}} \frac{h_{lk} \widetilde{C}_{lj}^1 \widetilde{C}_{kj}^2 \widetilde{C}_{\gamma\tau}^2}{\sigma_j^{12} \sigma_\tau^{12}}$$

$$\left. + \frac{1}{2} \sum_{\substack{\gamma\tau lkpqij \\ \tau\neq i,j}} \frac{\widetilde{C}_{li}^1 \widetilde{C}_{kj}^1 \widetilde{C}_{qj}^2 \widetilde{C}_{pi}^2 \widetilde{C}_{\gamma\tau}^2 \langle lk || pq \rangle}{\sigma_i^{12} \sigma_j^{12} \sigma_\tau^{12}} \right] \mathbf{D}_{\gamma\tau}^{\alpha\beta}. \quad (A14)$$

When the orbital overlap matrix s^{12} is singular, we present results in an appendix.

APPENDIX B: DENSITY MATRIX GRADIENTS FOR THE SINGULAR CASES

When orbital matrix s^{12} is singular, similar to Eq. (32), we can write down density matrix gradients according to number of singular values equal to zero. Note that in Eq. (A12), by applying general Frank–Condon rule to the expression, and subsequently combine with Eq. (A2), we reach the expression for density matrix gradients for the singular s^{12} cases as

$$
\frac{\partial \widetilde{H}_{12}}{\partial \mathbf{P}_1^{\alpha\beta}} =
\begin{cases}
\prod_{m\neq\mu} \sigma_m^{12} \Big[\sum_{\gamma k} h_{\gamma k}\widetilde{C}_{k\mu}^2 \mathbf{D}_{\gamma\mu}^{\alpha\beta} + \sum_{\gamma kpqj} \frac{\widetilde{C}_{kj}^1\widetilde{C}_{qj}^2\widetilde{C}_{p\mu}^2\langle\gamma k||pq\rangle \mathbf{D}_{\gamma\mu}^{\alpha\beta}}{\sigma_j^{12}} + \sum_{\gamma\tau kpq} \frac{\widetilde{C}_{k\mu}^1\widetilde{C}_{q\mu}^2\widetilde{C}_{p\tau}^2\langle\gamma k||pq\rangle \mathbf{D}_{\gamma\tau}^{\alpha\beta}}{\sigma_\tau^{12}} + \sum_{\substack{\gamma lkj \\ j\neq\mu}} \frac{h_{lk}\widetilde{C}_{lj}^1\widetilde{C}_{kj}^2\widetilde{C}_{\gamma\mu}^2 \mathbf{D}_{\gamma\mu}^{\alpha\beta}}{\sigma_j^{12}} + \sum_{\substack{\gamma\tau lk \\ \tau\neq\mu}} \frac{h_{lk}\widetilde{C}_{l\mu}^1\widetilde{C}_{k\mu}^2\widetilde{C}_{\gamma\tau}^2 \mathbf{D}_{\gamma\tau}^{\alpha\beta}}{\sigma_\tau^{12}} \\
\qquad + \frac{1}{2}\sum_{\substack{\gamma lkpqij \\ \mu\neq i,j}} \frac{\widetilde{C}_{li}^1\widetilde{C}_{kj}^1\widetilde{C}_{qj}^2\widetilde{C}_{pi}^2\widetilde{C}_{\gamma\mu}^2\langle lk||pq\rangle \mathbf{D}_{\gamma\mu}^{\alpha\beta}}{\sigma_i^{12}\sigma_j^{12}} \sum_{\substack{\gamma\tau lkpqi \\ \tau\neq i,\mu}} \frac{\widetilde{C}_{li}^1\widetilde{C}_{k\mu}^1\widetilde{C}_{q\mu}^2\widetilde{C}_{pi}^2\widetilde{C}_{\gamma\tau}^2\langle lk||pq\rangle \mathbf{D}_{\gamma\tau}^{\alpha\beta}}{\sigma_i^{12}\sigma_\tau^{12}} \Big], \quad \text{if} \quad \{\sigma_\mu^{12}=0\} \\[2em]
\prod_{m\neq\mu,\nu} \sigma_m^{12} \Big[\sum_{\gamma kpq} (\widetilde{C}_{k\mu}^1\widetilde{C}_{q\mu}^2\widetilde{C}_{p\nu}^2 \mathbf{D}_{\gamma\nu}^{\alpha\beta} + \widetilde{C}_{k\nu}^1\widetilde{C}_{q\nu}^2\widetilde{C}_{p\mu}^2 \mathbf{D}_{\gamma\mu}^{\alpha\beta})\langle\gamma k||pq\rangle + \sum_{\gamma lk} h_{lk}(\widetilde{C}_{l\mu}^1\widetilde{C}_{k\mu}^2\widetilde{C}_{\gamma\nu}^2 \mathbf{D}_{\gamma\nu}^{\alpha\beta} + \widetilde{C}_{l\nu}^1\widetilde{C}_{k\nu}^2\widetilde{C}_{\gamma\mu}^2 \mathbf{D}_{\gamma\mu}^{\alpha\beta}) + \sum_{\substack{\gamma\tau lkpq \\ \tau\neq\mu,\nu}} \frac{\widetilde{C}_{l\mu}^1\widetilde{C}_{k\nu}^1\widetilde{C}_{q\nu}^2\widetilde{C}_{p\mu}^2\langle lk||pq\rangle \widetilde{C}_{\gamma\tau}^2 \mathbf{D}_{\gamma\tau}^{\alpha\beta}}{\sigma_\tau^{12}} \\
\qquad + \sum_{\substack{\gamma lkpqi \\ i\neq\mu,\nu}} \frac{\widetilde{C}_{li}^1\widetilde{C}_{k\mu}^1\widetilde{C}_{q\mu}^2\widetilde{C}_{pi}^2\langle lk||pq\rangle \widetilde{C}_{\gamma\nu}^2 \mathbf{D}_{\gamma\nu}^{\alpha\beta}}{\sigma_i^{12}} + \sum_{\substack{\gamma lkpqi \\ i\neq\mu,\nu}} \frac{\widetilde{C}_{li}^1\widetilde{C}_{k\nu}^1\widetilde{C}_{q\nu}^2\widetilde{C}_{pi}^2\langle lk||pq\rangle \widetilde{C}_{\gamma\mu}^2 \mathbf{D}_{\gamma\mu}^{\alpha\beta}}{\sigma_i^{12}} \Big], \quad \text{if} \quad \{\sigma_\mu^{12}=\sigma_\nu^{12}=0\} \\[2em]
\prod_{m\neq\mu,\nu,\xi} \sigma_m^{12} \Big[\sum_{\gamma lkpq} \widetilde{C}_{l\nu}^1\widetilde{C}_{k\xi}^1\widetilde{C}_{q\xi}^2\widetilde{C}_{p\nu}^2\langle lk||pq\rangle \widetilde{C}_{\gamma\mu}^2 \mathbf{D}_{\gamma\mu}^{\alpha\beta} + \sum_{\gamma lkpq} \widetilde{C}_{l\mu}^1\widetilde{C}_{k\xi}^1\widetilde{C}_{q\xi}^2\widetilde{C}_{p\mu}^2\langle lk||pq\rangle \widetilde{C}_{\gamma\nu}^2 \mathbf{D}_{\gamma\nu}^{\alpha\beta} + \sum_{\gamma lkpq} \widetilde{C}_{l\nu}^1\widetilde{C}_{k\mu}^1\widetilde{C}_{q\mu}^2\widetilde{C}_{p\nu}^2\langle lk||pq\rangle \widetilde{C}_{\gamma\xi}^2 \mathbf{D}_{\gamma\xi}^{\alpha\beta} \Big], \quad \text{if} \quad \{\sigma_\mu^{12}=\sigma_\nu^{12}=\sigma_\xi^{12}=0\} \\[2em]
0, \quad \text{four or more zero singular values.}
\end{cases}
\tag{B1}
$$

[1] S. S. Iyengar and J. Jakowski, J. Chem. Phys. **122**, 114105 (2005).
[2] S. S. Iyengar, Theor. Chem. Acc. **116**, 326 (2006).
[3] J. Jakowski, I. Sumner, and S. S. Iyengar, J. Chem. Theory Comput. **2**, 1203 (2006).
[4] I. Sumner and S. S. Iyengar, J. Phys. Chem. A **111**, 10313 (2007).
[5] I. Sumner and S. S. Iyengar, J. Chem. Phys. **129**, 054109 (2008).
[6] S. S. Iyengar, I. Sumner, and J. Jakowski, J. Phys. Chem. B **112**, 7601 (2008).
[7] I. Sumner and S. S. Iyengar, J. Chem. Theory Comput. **6**, 1698 (2010).
[8] A. Pacheco and S. S. Iyengar, J. Chem. Phys. **133**, 044105 (2010).
[9] S. S. Iyengar, Int. J. Quantum Chem. **109**, 3798 (2009).
[10] J. C. Tully, Faraday Discuss. **110**, 407 (1998).
[11] R. Kapral and G. Ciccotti, J. Chem. Phys. **110**, 8919 (1999).
[12] I. Horenko, C. Salzmann, B. Schmidt, and C. Schutte, J. Chem. Phys. **117**, 11075 (2002).
[13] A. Donoso, Y. J. Zheng, and C. C. Martens, J. Chem. Phys. **119**, 5010 (2003).
[14] C. Brooksby and O. V. Prezhdo, Chem. Phys. Lett. **346**, 463 (2001).
[15] O. V. Prezhdo and C. Brooksby, Phys. Rev. Lett. **86**, 3215 (2001).
[16] E. Gindensperger, C. Meier, and J. A. Beswick, J. Chem. Phys. **113**, 9369 (2000).
[17] S. Hammes-Schiffer and J. Tully, J. Chem. Phys. **101**, 4657 (1994).
[18] Y. Chan, *Wavelet Basics* (Kluwer Academic, 1995).
[19] I. Daubechies, *Ten Lectures in Wavelets* (SIAM, Philadelphia, PA, 1992).
[20] G. Strang and T. Nguyen, *Wavelets and Filter Banks* (Wellesley-Cambridge, 1996).
[21] G. Strang and V. Strela, Opt. Eng. **33**, 2104 (1994).
[22] T. Arias, Rev. Mod. Phys. **71**, 267 (1999).
[23] B. R. Johnson, J. P. Modisette, P. J. Nordlander, and J. L. Kinsey, J. Chem. Phys. **110**, 8309 (1999).
[24] G. W. Wei, D. S. Zhang, D. K. Kouri, and D. J. Hoffman, Phys. Rev. Lett. **79**, 775 (1997).
[25] D. K. Hoffman, G. W. Wei, D. S. Zhang, and D. J. Kouri, Phys. Rev. E **57**, 6152 (1998).
[26] W. H. Press, S. A. Teukolsky, W. T. Vetterling, and B. P. Flannery, *Numerical Recipes in C* (Cambridge University Press, New York, 1992).
[27] X. Li and S. S. Iyengar, http://www.indiana.edu/ssiweb/papers/sadafp.pdf.
[28] I. Sumner, P. Phatak, and S. S. Iyengar (in preparation).
[29] S. Yamanaka, S. Nishihara, K. Nakata, Y. Yonezawa, M. Okumura, T. Takada, H. Nakamura, and K. Yamaguchi, Int. J. Quantum Chem. **109**, 3811 (2009).
[30] R. L. Martin, J. Chem. Phys. **74**, 1852 (1981).
[31] A. F. Voter and W. A. Goddard III, Chem. Phys. **57**, 253 (1981).
[32] C. F. Jackels and E. R. Davidson, J. Chem. Phys. **64**, 2908 (1976).
[33] A. J. W. Thom and M. Head-Gordon, J. Chem. Phys. **131**, 124113 (2009).
[34] Q. Wu, C.-L. Cheng, and T. Van Voorhis, J. Chem. Phys. **127**, 164119 (2007).
[35] J. Skone, M. Pak, and S. Hammes-Schiffer, J. Chem. Phys. **123**, 134108 (2005).
[36] P. Y. Ayala and H. B. Schlegel, J. Chem. Phys. **108**, 7560 (1998).
[37] M. F. Trotter, Proc. Am. Math. Soc. **10**, 545 (1959).
[38] E. Nelson, J. Math. Phys. **5**, 332 (1964).
[39] Y. Huang, D. J. Kouri, M. Arnold, I. Thomas, L. Marchioro, and D. K. Hoffman, Comput. Phys. Commun. **80**, 1 (1994).
[40] D. K. Hoffman, N. Nayar, O. A. Sharafeddin, and D. J. Kouri, J. Phys. Chem. **95**, 8299 (1991).
[41] D. J. Kouri, Y. Huang, and D. K. Hoffman, Phys. Rev. Lett. **75**, 49 (1995).
[42] C. Swalina and S. Hammes-Schiffer, J. Phys. Chem. A **109**, 10410 (2005).
[43] R. B. Gerber and M. A. Ratner, J. Chem. Phys. **70**, 97 (1988).
[44] N. Matsunaga, G. M. Chaban, and R. B. Gerber, J. Chem. Phys. **117**, 3541 (2002).
[45] X. Li, J. Oomens, J. R. Eyler, D. T. Moore, and S. S. Iyengar, J. Chem. Phys. **132**, 244301 (2010).
[46] D. Hocker, X. Li, and S. S. Iyengar, "Shannon information entropy based time-dependent deterministic sampling techniques for efficient on-the-fly quantum dynamics and electronic structure," J. Chem. Phys. (submitted).
[47] C. Shannon, Bell Syst. Tech. J. **27**, 279 (1948).
[48] C. Shannon, Proc. IEEE **86**, 447 (1998).
[49] R. McWeeny, Rev. Mod. Phys. **32**, 335 (1960).
[50] A. J. W. Thom and M. Head-Gordon, Phys. Rev. Lett. **101**, 193001 (2008).
[51] G. H. Golub and C. F. van Loan, *Matrix Computations* (The Johns Hopkins University Press, Baltimore, 1996).
[52] S. T. Roweis and L. K. Saul, Science **290**, 2323 (2000).
[53] J. Tenenbaum, *Neural Information Processing* (MIT Press, Cambridge, MA, 1988), pp. 682–688.
[54] B. Roos, *Theory and Applications of Computational Chemistry: The First 40 Years* (Elsevier Science, 2005).
[55] M. Baer, *Beyond Born–Oppenheimer: Electronic Nonadiabatic Coupling Terms and Conical Intersections* (Wiley, New York, 2006).
[56] G. Hanna and R. Kapral, Acc. Chem. Res. **39**, 21 (2006).
[57] G. A. Worth and L. S. Cederbaum, Annu. Rev. Phys. Chem. **55**, 127 (2004).
[58] A. W. Jasper, C. Zhu, S. Nangia, and D. G. Truhlar, Faraday Discuss. **127**, 1 (2004).
[59] B. K. Kendrick, C. A. Mead, and D. G. Truhlar, Chem. Phys. **277**, 31 (2002).
[60] A. Kuppermann, *Dynamics of Molecules and Chemical Reactions* (Mar-

cel Dekker, New York, NY, 1996), pp. 411–472.

[61] D. R. Yarkony, Rev. Mod. Phys. **68**, 985 (1996).

[62] S. Matsika and D. R. Yarkony, J. Am. Chem. Soc. **125**, 10672 (2003).

[63] H. B. Schlegel, J. M. Millam, S. S. Iyengar, G. A. Voth, A. D. Daniels, G. E. Scuseria, and M. J. Frisch, J. Chem. Phys. **114**, 9758 (2001).

[64] S. S. Iyengar, H. B. Schlegel, J. M. Millam, G. A. Voth, G. E. Scuseria, and M. J. Frisch, J. Chem. Phys. **115**, 10291 (2001).

[65] H. B. Schlegel, S. S. Iyengar, X. Li, J. M. Millam, G. A. Voth, G. E. Scuseria, and M. J. Frisch, J. Chem. Phys. **117**, 8694 (2002).

[66] S. S. Iyengar, H. B. Schlegel, G. A. Voth, J. M. Millam, G. E. Scuseria, and M. J. Frisch, Isr. J. Chem. **42**, 191 (2002).

[67] S. S. Iyengar, M. K. Petersen, T. J. F. Day, C. J. Burnham, V. E. Teige, and G. A. Voth, J. Chem. Phys. **123**, 084309 (2005).

[68] S. S. Iyengar, J. Chem. Phys. **126**, 216101 (2007).

[69] S. S. Iyengar, T. J. F. Day, and G. A. Voth, Int. J. Mass. Spectrom. **241**, 197 (2005).

[70] S. S. Iyengar, J. Chem. Phys. **123**, 084310 (2005).

[71] X. Li, V. E. Teige, and S. S. Iyengar, J. Phys. Chem. A **111**, 4815 (2007).

[72] X. Li, D. T. Moore, and S. S. Iyengar, J. Chem. Phys. **128**, 184308 (2008).

[73] R. S. Mulliken, J. Chem. Phys. **61**, 20 (1964).

[74] A. Warshel and R. M. Weiss, J. Am. Chem. Soc. **102**, 6218 (1980).

[75] Y.-T. Chang and W. H. Miller, J. Phys. Chem. **94**, 5884 (1990).

[76] D. Borgis and A. Staib, Chem. Phys. Lett. **238**, 187 (1995).

[77] T. J. F. Day, A. V. Soudachov, M. Cuma, U. W. Schmidt, and G. A. Voth, J. Chem. Phys. **117**, 5839 (2002).

[78] W. A. Goddard III, Phys. Rev. **157**, 73 (1967).

[79] J. Gerratt, D. L. Cooper, P. B. Karadakov, and M. Raimondi, Chem. Soc. Rev. **26**, 87 (1997).

[80] A. Szabo and N. Ostlund, *Modern Quantum Chemistry: Introduction to Advanced Electronic Structure Theory*, 1st ed. (Dover, New York, 1996).

[81] T. Helgaker, P. Jørgensen, and J. Olsen, *Molecular Electronic-Structure Theory* (Wiley, New York, 2000).

[82] P. A. M. Dirac, *The Principles of Quantum Mechanics*, The International Series of Monographs on Physics Vol. 27, 4th ed. (Oxford University Press, New York, 1958).

[83] A. T. Amos and G. G. Hall, Proc. R. Soc. London, Ser. A **263**, 483 (1961).

[84] P.-O. Löwdin, J. Appl. Phys. **33**, 251 (1962).

[85] P.-O. Löwdin, Phys. Rev. **97**, 1490 (1955).

[86] W. A. Goddard III, J. Chem. Phys. **48**, 450 (1968).

[87] P.-O. Löwdin, Phys. Rev. **97**, 1474 (1955).

[88] G. E. Scuseria, J. Phys. Chem. A **103**, 4782 (1999).

[89] W. Yang, Phys. Rev. Lett. **66**, 1438 (1991).

[90] S. Goedecker, Rev. Mod. Phys. **71**, 1085 (1999).

[91] C. A. White and M. Head-Gordon, J. Chem. Phys. **101**, 6593 (1994).

[92] M. C. Strain, G. E. Scuseria, and M. J. Frisch, Science **271**, 51 (1996).

[93] X. P. Li, W. Nunes, and D. Vanderbilt, Phys. Rev. B **47**, 10891 (1993).

[94] J. M. Millam and G. E. Scuseria, J. Chem. Phys. **106**, 5569 (1997).

[95] A. D. Daniels, J. M. Millam, and G. E. Scuseria, J. Chem. Phys. **107**, 425 (1997).

[96] S. Rothenberg and H. F. Schaefer III, J. Chem. Phys. **54**, 2764 (1971).

[97] F.-M. Tao and Y.-K. Pan, J. Chem. Phys. **97**, 4989 (1992).

[98] F.-M. Tao, J. Chem. Phys. **98**, 2481 (1993).

[99] H. L. Williams, E. M. Mas, K. Szalewicz, and B. Jeziorski, J. Chem. Phys. **103**, 7374 (1995).

[100] H. Ichikawa, H. Kagawa, and C. Kaneko, Bull. Chem. Soc. Jpn. **73**, 2001 (2000).

[101] J. M. L. Martin, J. P. François, and R. Gijbels, J. Comput. Chem. **10**, 875 (1989).

[102] P. Pulay, Mol. Phys. **17**, 197 (1969).

[103] K. Kawaguchi, J. Chem. Phys. **88**, 4186 (1988).

[104] C. Swalina, M. V. Pak, and S. Hammes-Schiffer, Chem. Phys. Lett. **404**, 394 (2005).

[105] A. B. McCoy, J. Chem. Phys. **103**, 986 (1995).

[106] P. Botschwina, P. Sebal, and R. Burmeister, J. Chem. Phys. **88**, 5246 (1988).

[107] R. B. Metz, T. Kitsopoulos, A. Weaver, and D. Neumark, J. Chem. Phys. **88**, 1463 (1988).

[108] M. G. Del Pópolo, J. Kohanoff, and R. M. Lynden-Bell, J. Phys. Chem. B **110**, 8798 (2006).

[109] O. Mó, M. Yáñez, J. E. Del Bene, I. Alkorta, and J. Elguero, ChemPhysChem **6**, 1411 (2005).

[110] R. T. Pack and G. A. Parker, J. Chem. Phys. **87**, 3888 (1987).

[111] S. Carter and J. M. Bowman, J. Chem. Phys. **108**, 4397 (1998).

[112] S. S. Iyengar, G. A. Parker, D. J. Kouri, and D. K. Hoffman, J. Chem. Phys. **110**, 10283 (1999).

[113] A. Kuppermann, J. Phys. Chem. A **113**, 4518 (2009).

[114] M. J. Frisch, G. W. Trucks, H. B. Schlegel *et al.*, Gaussian Development Version, Revision b.01, Gaussian, Inc., Pittsburgh, PA.

[115] A. D. Becke, J. Chem. Phys. **88**, 2547 (1988).

[116] V. I. Lebedev, Zh. Vychisl. Mat. Mat. Fiz. **15**, 48 (1975).

[117] V. I. Lebedev, Zh. Vychisl. Mat. Mat. Fiz. **16**, 293 (1976).

[118] V. I. Lebedev and L. Skorokhodov, Russian Acad., Sci. Dokl. Math. **45**, 587 (1992).

[119] K. D. Kreuer, A. Fuchs, M. Ise, M. Spaeth, and J. Maier, Electrochim. Acta **43**, 1281 (1998).

[120] M. E. Tuckerman, D. Marx, and M. Parrinello, Nature (London) **417**, 925 (2002).

[121] D. Marx, M. E. Tuckerman, J. Hutter, and M. Parrinello, Nature (London) **397**, 601 (1999).

[122] D. Asthagiri, L. R. Pratt, J. D. Kress, and M. A. Gomez, Proc. Natl. Acad. Sci. U.S.A. **101**, 7229 (2004).

[123] J.-W. Shin, N. I. Hammer, E. G. Diken, M. A. Johnson, R. S. Walters, T. D. Jaeger, M. A. Duncan, R. A. Christie, and K. D. Jordan, Science **304**, 1137 (2004).

[124] E. G. Diken, J. M. Headrick, J. R. Roscioli, J. C. Bopp, M. A. Johnson, A. B. McCoy, X. Huang, S. Carter, and J. M. Bowman, J. Phys. Chem. A **109**, 571 (2005).

[125] N. I. Hammer, E. G. Diken, J. R. Roscioli, M. A. Johnson, E. M. Myshakin, K. D. Jordan, A. B. McCoy, X. Huang, J. M. Bowman, and S. Carter, J. Chem. Phys. **122**, 244301 (2005).